

**Development, Implementation And Validation Of In-Situ Raman Hot  
Stage Reactor**

By  
Khaled Khalili

A thesis submitted in partial fulfillment of the requirements for the degree of  
Master of Science  
in  
Chemical Engineering

Department of Chemical & Material Engineering  
University of Alberta

© Khaled Khalili, 2014

## Abstract

In the upgrading of heavy feeds, it is essential to avoid the onset formation of mesophase, which is considered a precursor for coke formation. The formation of this aromatic dense phase leads to serious problems such as catalyst deactivation, limiting the vacuum residue conversion, and fouling in the reactors and the downstream equipment; subsequently, a costly mechanical removal will be necessary to remove the coke. Therefore, tracking of the mesophase formation at *in-situ* conditions is an important step towards avoiding the onset formation of carbonaceous mesophase.

In this work, a fiber-coupled *in-situ* Raman hot reactor was designed, constructed and validated. The system has been developed as an on-line chemical sensor to track evolution of the two graphitization Raman bands associated with the mesophase formation, namely the  $1575\text{cm}^{-1}$  band and the band located near  $1340\text{cm}^{-1}$ . The operation of the system is based on acquiring real-time backscattered Raman spectra from a hot stage reactor running at high temperature and sometimes high-pressure conditions.

The outcome of this system has been validated using non-reactive and reactive systems. In terms of non-reactive systems, the spectra of some common solvents such as toluene and 1-methylnaphthalene have been acquired using this system and then compared with the published spectra; excellent spectral matching in the range of  $\pm 5\text{cm}^{-1}$  is observed. On the other hand, the hydro-desulfurization reaction of benzothiophene using 1-methylnaphthalene as a solvent has been used as a model reaction for system validation. This reaction has been conducted *ex-situ* and *in-situ* at the same experimental conditions i.e.  $290^\circ\text{C}$  and 2.5 MPa of hydrogen pressure. The GC/MS analysis of the *ex-situ* shows hydrodesulphurization of benzothiophene and formation of ethylbenzene, which is in agreement with the well-known chemistry of this reaction; in addition, a considerable

hydrogenation of the solvent was observed in the products of the *ex-situ* runs, which confirms the hydrogenation capability of the used catalyst. The spectral data, which have been acquired during the *in-situ* runs, have been preprocessed using the airPLS algorithm to remove the fluorescence background from the spectra that have been then analyzed using multivariate PCA analysis. The PCA analysis confirms the evolution of the Raman bands associated with ethylbenzene formation and the decline of the Raman bands attributed to benzothiophen; moreover, the PCA analysis also shows a concomitant decrease of the aromatic content of the mixture via hydrogenation of aromatic rings which confirms the hydrogenation of the solvent that have been observed in the *ex-situ* runs.

# Table Of Content

<b>CHAPTER 1: INTRODUCTION.....</b>	<b>1</b>
<b>CHAPTER 2: LITERATURE REVIEW .....</b>	<b>3</b>
2.1 MESOPHASE FORMATION.....	3
2.2 <i>EX-SITU</i> RAMAN MEASUREMENTS OF THE CARBONACEOUS MESOPHASE.....	5
2.3 UPGRADING BY HYDROTREATING .....	6
2.3.1 <i>Hydrodesulfurization (HDS)</i> .....	6
2.3.2 <i>Hydrodesulfurization Of Benzothiophene</i> .....	6
<b>CHAPTER 3: RAMAN SPECTROSCOPY-BASIC PRINCIPLES .....</b>	<b>8</b>
3.1 LIGHT .....	8
3.2 DEGREES OF FREEDOM FOR MOLECULAR VIBRATIONS .....	9
3.3 RAMAN SCATTERING PROCESS.....	10
3.4 IR SPECTROSCOPY VS. RAMAN SPECTROSCOPY.....	14
3.5 INTENSITY OF RAMAN SIGNAL .....	17
3.6 DEPOLARIZATION RATIO .....	19
<b>CHAPTER 4: INSTRUMENTATION AND SYSTEM DEVELOPMENT .....</b>	<b>21</b>
4.1 IN-SITU RAMAN HOT STAGE REACTOR: THE BASIC ITEMS .....	21
4.2 SYSTEM SAFETY .....	24
<i>A. Engineering Control Measures</i> .....	25
<i>B. Protective Equipment Measures</i> .....	26
<i>C. Administrative Control Measures</i> .....	26
4.3 SYSTEM DESIGN.....	28
4.3.1 <i>Hot Stage Reactor Design</i> .....	28
4.3.1.1 Overview.....	28
4.3.1.2 Reactor Design .....	30
4.3.1.3 Mixing System .....	32
4.3.1.4 Heating System.....	33
4.3.2 <i>Laser Source</i> .....	35
4.3.3 <i>Spectrometer</i> .....	39
4.3.3.1 Monochromator Vs. Spectrograph .....	39
4.3.3.2 Spectrometer Efficiency .....	42
4.3.3.3 Detectors.....	43
4.3.3.4: The Selected Spectrometer.....	44
4.3.4 <i>Sample Illumination And Collection System</i> .....	46
A. The Polarization Probe .....	46
B. Excitation And Collection Fiber Optics.....	48
C. Three-Dimensional Motorized Stage.....	48
<b>CHAPTER 5: MATERIALS AND METHODOLOGY.....</b>	<b>50</b>
5.1 MATERIALS AND CHEMICALS .....	50
5.2 METHODOLOGY .....	51
5.3 EXPERIMENTAL PROCEDURES.....	51
5.3.1 <i>Preliminary Acquisition Procedures</i> .....	51
5.3.1.1 Laser-Sample Alignment.....	52
5.3.1.2 Optimum Acquisition Parameters.....	52
5.3.1.3 Subtraction of Dark Spectrum.....	53
5.3.2 <i>Validating Raman Spectra For Non-Reactive Systems</i> .....	53
5.3.3 <i>Establishing Spectral Calibration Curve For Quantitative Analysis</i> .....	54
5.3.4 <i>Ex-Situ HDS Reaction Of BT</i> .....	54

5.3.5 <i>In-situ HDS Reaction of BT</i> .....	55
5.3.6 <i>Products Analysis</i> .....	58
<b>CHAPTER 6: RESULTS AND DISCUSSION</b> .....	<b>59</b>
6.1 PREPROCESSING OF SPECTRAL DATA.....	59
6.2 VALIDATING THE COLLECTED RAMAN SPECTRA.....	61
6.3 SPECTRAL CALIBRATION CURVE FOR QUANTITATIVE ANALYSIS.....	63
6.3 HDS REACTION OF BT.....	66
6.3.1 <i>Multivariate Analysis</i> .....	66
6.3.2 <i>In-situ HDS Reaction of BT</i> .....	69
6.3.2.1 Raman Activity In 450-830 $\text{Cm}^{-1}$ Region.....	72
6.3.2.2 Raman Activity In 830-1100 $\text{Cm}^{-1}$ Region.....	75
6.3.2.3 Raman Activity In 1150-1650 $\text{Cm}^{-1}$ Region.....	78
6.3.3 <i>Products Analysis</i> .....	82
6.3.3.1 Product Analysis Of The Ex-Situ Reactions.....	82
6.3.3.2 Product Analysis Of The In-Situ Reactions.....	84
<b>CONCLUSION</b> .....	<b>85</b>
<b>BIBLIOGRAPHY</b> .....	<b>ERROR! BOOKMARK NOT DEFINED.</b>

## List of Figures

Figure 2.1: Proposed routes for HDS of BT.	7
Figure 3.1: Schematic of plain polarized light.	9
Figure 3.2: Temporary dipole moment of a homo-nuclear diatomic molecule induced by the external electric field of incident light.	12
Figure 3.3: Collision model of light scattering.	13
Figure 3.4: Schematic for energy levels involved in scattering.	14
Figure 3.5: Modes of vibration for CO <sub>2</sub> .	17
Figure 3.6: Schematic of parallel (black) and perpendicular (green) components of scattered light.	20
Figure 4.1: Typical arrangement of Raman system.	22
Figure 4.2: In-situ Raman hot stage reactor	24
Figure 4.3: (a) Hot stage reactor used by Rahimi et al., (b) New hot stage reactor used by Bagheri	30
Figure 4.4: (a) Schematic of the reactor with a square surrounding the lower part that consists of Parker fittings. (b) Detailed schematic of the reactor excepting the Parker part	31
Figure 4.5: Lower part reactor assembly	32
Figure 4.6: Custom-made Alnico magnet block	33
Figure 4.7: Schematic for the lower part of the reactor with the magnetic stirrer.	34
Figure 4.8: (a) wrapping steel foam around the reactor, (b) wrapping the	35

heating tape over the steel foam.

Figure 4.9: Top view of the fiber coupled 785nm Raman Laser. Module from RGBlase LLC.	39
Figure 4.10: Schematic of diffraction grating.	41
Figure 4.11: Schematic of double monochromator.	42
Figure 4.12: Schematic of Czerny-Turner spectrograph.	43
Figure 4.13: Schematic of CCD detector.	45
Figure 4.14: Quantum efficiency curve for back-thinned CCDs detector from Hamamatsu, model S7031-1006.	46
Figure 4.15: Sketch of the polarization probe	48
Figure 4.16: The polarization probe mounted on the motorized stage	50
Figure 5.1: The micro-batch reactor that has been used for ex-situ reactions.	56
Figure 5.2: The micro-batch reactor emerged into hot sand reciprocal saw shaker.	56
Figure 5.3: Wrapping the insulation material over the heating tape.	58
Figure 5.4: The hot stage reactor mounted over the polarization probe.	58
Figure 6.1: Original and baseline corrected spectrum using CWT and airPLS algorithms	62
Figure 6.2: (a) Toluene spectrum published in SDBS; (b) Toluene spectrum acquired by the implemented Raman system.	63
Figure 6.3: (a) Raman spectra of toluene in dodecane mixtures in the range of (0 – 12 wt.%); (b) a zoomed in region of the $628\text{ cm}^{-1}$ unique toluene	65

band.

Figure 6.4: The height of the  $628\text{ cm}^{-1}$  peak vs. toluene concentration. 66

Figure 6.5: Three-dimensional plot of on-line Raman baseline corrected spectra for one of HDS reaction of BT. 67

Figure 6.6: (a) The loading of PC1 vs. wavenumbers; (b) the scores of PC1 vs. time. ( $200\text{-}2000\text{ cm}^{-1}$  range). 69

Figure 6.7: Scree plot of total variance described by each PC ( $200\text{-}2000\text{ cm}^{-1}$  range). 70

Figure 6.8: (a) The loading of PC1 vs. wavenumbers; (b) the scores of PC1 vs. time. ( $450\text{-}830\text{ cm}^{-1}$  range). 73

Figure 6.9: Scree plot of total variance described by each PC ( $450\text{-}830\text{ cm}^{-1}$  range). 74

Figure 6.10: (a) The loading of PC1 vs. wavenumbers; (b) the scores of PC1 vs. time. ( $450\text{-}830\text{ cm}^{-1}$  range). 75

Figure 6.11: (a) The loading of PC1 vs. wavenumbers; (b) the scores of PC1 vs. time. ( $830\text{-}1110\text{ cm}^{-1}$  range). 77

Figure 6.12: (a) The loading of PC1 vs. wavenumbers; (b) the scores of PC1 vs. time. ( $830\text{-}1100\text{ cm}^{-1}$  range). 78

Figure 6.13: Scree plot of total variance described by each PC ( $830\text{-}1100\text{ cm}^{-1}$  range) 79

Figure 6.14: Scree plot of total variance described by each PC ( $1330\text{-}1660\text{ cm}^{-1}$  range) 79

Figure 6.15: (a) The loading of PC1 vs. wavenumbers; (b) the scores of 80



PC1 vs. time. (1150-1650  $\text{cm}^{-1}$  range)

Figure (6.16): (a) The loading of PC2 vs. wavenumbers; (b) the scores of

PC2 vs. time. (1150-1650  $\text{cm}^{-1}$  range)

82

## **List of Tables**

Table 6.1: Raman shifts for BT, 1-Methylnaphthalene and EB	72
Table 6.2: Products analyses for the ex-situ run after 4 hours of reaction	84

## Chapter 1: Introduction

Carbonaceous mesophase is the aromatic dense phase that is formed upon the heat treatment of petroleum pitches in the temperature range 350-500 °C<sup>1</sup>. The formation of the mesophase in the upgrader limits the vacuum residue conversion, leads to catalyst deactivation and fouling in the reactors and the downstream equipment.

Mesophase formation phenomena in petroleum pitches has been studied using different techniques, such as polarized optical microscopy coupled with a hot stage reactor<sup>1</sup>, high temperature X-ray diffraction, high temperature C-NMR<sup>2</sup>, Transmission electron microscopy<sup>3</sup> and *ex-situ* Raman microscopy<sup>4</sup>. Due to the complex chemical and physical processes associated with mesophase formation and due to the limitations associated with each of the previously mentioned analytical techniques, it is still not possible to completely elucidate the exact mechanism of mesophase formation. One example is the problems associated with the study of mesophase growth using a hot stage reactor coupled with polarized optical microscopy; while the system allows the reaction to be followed at real-time conditions; the lower size limit of observation is only 0.5 microns due to the relatively low resolution of optical microscopy. If mesophase domains with sizes smaller than the lower detection limit of the microscope, the reacting mixture will appear as an isotropic liquid<sup>1</sup>. On the other hand, transmission electron microscopy offers higher resolution down to 0.1 micron<sup>3</sup> but other operational problems prevent this technique from being used at higher temperatures.

To fully investigate the mesophase formation, it is required to have a tool that offers the following essential features:

- High resolution down to molecular level to reveal the chemistry involved in the process
- Based on polarization of light since the mesophase is characterized by its anisotropy
- Observable at real time conditions of temperature and pressure.

One method that satisfies this wish-list is *in-situ* Raman microscopy. Raman spectroscopy has been named after Sir Chandrasekhra Venkata Raman who discovered

the phenomena in 1928<sup>5,6</sup>. The Raman effect and the IR absorption process together form the discipline of vibrational spectroscopy that is very useful in studying the molecular structure. The IR and Raman processes are complementary techniques and both processes provide information about the chemical structure. Although both processes arise from totally different mechanism they both produce vibrations in the same spectral range namely the Mid-IR and Near-IR ranges. The Raman spectroscopy has become a powerful analytical tool since 1990s due to the introduction of high efficiency laser sources, sensitive detectors, fiber optics and fast computers<sup>6,7</sup>. Interfacing the fiber optics with the laser source and the spectrometer allows acquiring Raman spectra for remote-harsh environments at real time conditions which are not generally possible using IR spectroscopy<sup>8</sup>.

As mentioned earlier, *ex-situ* Raman spectroscopy has been used to study samples of mesophase petroleum pitches<sup>4</sup>; however, it is extremely difficult to assign the Raman bands observed at *ex-situ* conditions to the observed *in-situ* bands that are associated with the structural changes happened during the mesophase formation since both measurements are done at different conditions. Therefore, the objective of this work is to build and validate analytical tool that can track the evolution of chemical structure at real-time conditions. For this thesis, a hot stage reactor coupled with *in-situ* Raman microscopy has been developed, implemented and validated.

## Chapter 2: Literature Review

This literature review covers the concept of carbonaceous mesophase and the qualitative characteristic techniques that have been used to understand the mechanism of this phenomenon. In addition, two *ex-situ* Raman measurements of the carbonaceous mesophase are reported. After that, the hydro-treatment process as an upgrading technology to suppress the mesophase formation in the heavy feed is covered. The concept of hydro-treatment process is then extended to cover the well-known hydrodesulfurization reaction of benzothiophene as a model reaction that has been used in this study to validate the outcome of the implemented system.

### 2.1 Mesophase Formation

Carbonaceous mesophase is considered to be an intermediate state of matter between conventional liquid and conventional solid because it moves like a liquid and has an orientational molecular character like solid. The carbonaceous mesophase is further characterized by its optical anisotropy when viewed with polarized optical microscopy. In this particular system, the mesophase appears as an anisotropic phase surrounded by isotropic phase<sup>1</sup>; therefore, the polarized optical microscope is a powerful tool to investigate the formation of this phase.

Different mechanisms have been proposed to describe the mesophase formation such as solubility, stability, precipitation, crystallization and molecular self-assembly<sup>1</sup>; however, it is widely agreed that mesophase formation is due to a complex combination between chemical reactions and phase separation. Riggs and Diefendorf represented the mesophase as a mixture of mesogens and non-mesogenic molecules<sup>1</sup>. The mesogens are proposed to be large aromatic disk-like molecules while the non-mesogens are the medium of smaller solvent-like molecules. Mochida and Korai prepared a partial phase

diagram for mesophase formation by mixing benzene soluble fractions with benzene insoluble fractions of coal tar pitch at different ratios and studying them using hot stage microscope <sup>1</sup>. Care must be taken in interpreting these concepts because mesophase formation is not always reversible.

Mochida and co-workers<sup>9</sup> in their paper about the synthesis chemistry of aromatic-derived mesophase, outlined the formation mechanism of a carbon-rich material. They proposed that the aromatic molecules are assembled to form clusters, which then stack together to form micro-domains; these micro-domains are arranged into larger domains that form the building blocks of the carbon material.

Wiehe<sup>10</sup> proposed the concept of solubility to explain the liquid-liquid phase separation that occurs during the mesophase formation. He proposed that the mesophase separation from the liquid phase was due to the combined effect of free radical addition reactions and the solubility limit of the solution. The addition reactions create heavy aromatic molecules in the liquid phase that oligomerize until the solubility limit of these molecules exceed the solubility limit of the whole solution. Marsh and coworkers<sup>11</sup> proposed, however, that the higher stability of the mesophase is the reason of the separation of the mesophase from the liquid phase not the solubility limit as proposed by Wiehe.

Because the mesophase is the dominant factor in determining the performance of the carbonaceous materials such as carbon fibers and carbon composites, the mesophase formation have been frequently studied by different techniques. Mochida and Korai<sup>2</sup> used polarized optical microscopy coupled with a hot stage reactor to study the formation of solid mesophase. They found that the performance of carbon materials is related to the degree of ordered stacking of the aromatic planes along the fiber axis. On the other hand,

Mochida and Korai<sup>2</sup> also studied the fused mesophase using a high temperature X-ray diffractometer ( XRD) and high temperature <sup>13</sup>C-NMR. They reported a broader peak position of the C(002) X-ray diffraction profile with a shift to lower angles when the temperature was increasing to 400°C. Moreover, in their high temperature <sup>13</sup>C-NMR study, they reported that the aligned carbons shifted slightly to the higher magnetic field when the temperature was increased which is an indication of a thinner layer of the stacked aromatic molecules while the unaligned aromatic carbon didn't change.

## **2.2 *Ex-situ* Raman Measurements Of the Carbonaceous Mesophase**

Angell and Lewis<sup>4</sup> have reported *ex-situ* measurements for a range of mesophase pitches from different starting materials prepared by pyrolysis at 400 to 450 °C in an inert atmosphere. They observed two Raman bands; the first band is located in the 1595 to 1610 cm<sup>-1</sup> range which are attributed to the aromatic hexagonal network of the graphene<sup>4</sup>. They correlated the lower wavenumber limit with better perfection in the hexagonal aromatic network since the single crystal graphite have a single Raman band at 1575 cm<sup>-1</sup><sup>4</sup>. The second Raman band is situated between 1330 to 1350 cm<sup>-1</sup>, but the origin on this band is not completely understood<sup>4</sup>. Zhou and co-workers<sup>12</sup> have studied the effect of ferrous-nickel alloy catalyst on the degree of graphitization of heat-treated carbon fibers using Raman spectroscopy. They have specified two Raman bands associated with the degree of graphitization: the D-band located around 1340 cm<sup>-1</sup> and the G-band located at 1575 cm<sup>-1</sup>. They have attributed the D-band to the degree of disorder in carbon fibers and the G-band to the degree of graphitization perfection. Zhou and co-workers<sup>12</sup> have reported that the catalytic graphitization of carbon pitch have enhanced the degree of graphitization at lower temperatures.

## 2.3 Upgrading By Hydrotreating

The hydrotreating process is the standard process for improving the lower value sour oils into higher value streams. Hydrotreating utilizes high pressure hydrogen and catalysts at temperatures below the thermal cracking limit to remove the heteroatoms such as sulfur, nitrogen and metal and to decrease the aromatic content of the feed<sup>13</sup>. The catalytic process of removing sulfur by hydrogen is called hydrodesulfurization (HDS), while the hydrodenitrogenation (HDN) and the hydrodemetalization (HDM) processes are the processes for removing nitrogen and metals respectively. These catalytic processes are important to decrease the sulfur and nitrogen emission upon fuel combustion; furthermore, hydrotreating is important to suppress the coke formation in the reactor and in the downstream equipment. However, the major challenge of the hydrotreating process is the catalyst deactivation due to the deposition of metals and coke on the surface of the catalyst<sup>13</sup>.

### 2.3.1 Hydrodesulfurization (HDS)

There are two forms of sulfur in crude oil: the thiophenic sulfur and the aliphatic sulfur. The aliphatic sulfur is much easier to be removed due to the open-ended structure of the sulfur atom, while the thiophenic sulfur are less reactive and much more difficult to remove due to the presence of the sulfur atom in five membered ring structure<sup>13</sup>. Sulfided NiMo and CoMo supported on  $\gamma$ -Al<sub>2</sub>O<sub>3</sub> are the typical catalysts used in upgrading of oil feedstock; however, the sulfided NiMo is more selective to hydrogenation/hydrodenitrogenation pathways while the sulfided CoMo catalyst is more selective towards the desulfurization pathway<sup>13</sup>.

### 2.3.2 Hydrodesulfurization Of Benzothiophene

The benzothiophene (BT) is an example of thiophenic sulfur present in crude oil. Shi and co-workers<sup>14</sup> have studied the HDS of BT over NiMo/  $\gamma$ -Al<sub>2</sub>O<sub>3</sub> catalyst in a flow micro-reactor at temperatures ranging from 180 to 260 °C and 2 MPa of hydrogen pressure, at different hourly space time velocities. They proposed two reaction routes; the first route



is via the hydrogenation of BT into dihydrobenzothiophene (DHBT); the second route is via direct cleavage of sulfur from the aromatic ring into styrene (ST) which is considered as intermediate that readily reacted into ethylbenzene (EB). Figure (2.1) shows the two proposed routes for HDS of BT.

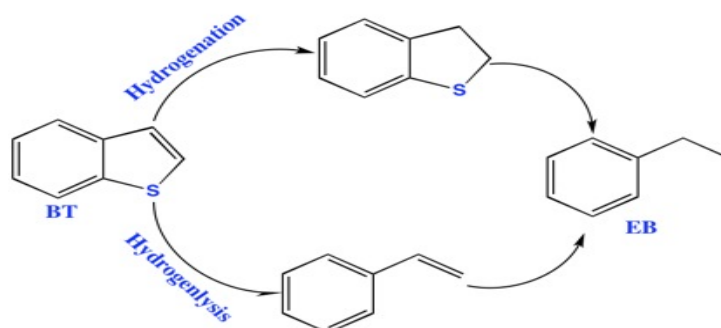


**Figure 2.1: Proposed routes for HDS of BT**

Wang and Prins<sup>15</sup> have investigated the HDS mechanism of BT and DHBT over sulfided Mo/  $\gamma$ -Al<sub>2</sub>O<sub>3</sub> catalyst at 5 MPa of hydrogen pressure and 280 to 300 °C. They also have proposed two reaction mechanisms; the first mechanism is via the hydrogenolysis of BT into styrene (sulfur-carbon cleavage reaction) followed by direct hydrogenation of styrene into EB; the second mechanism is via hydrogenation of BT into DHBT which is then converted by hydrogenolysis into EB. They used the less active Mo/  $\gamma$ -Al<sub>2</sub>O<sub>3</sub> catalyst in order to see more intermediates and to have better understanding of the underlying reaction mechanisms. Wang and Prins<sup>15</sup> reported better hydrogenolysis selectivity over hydrogenation at higher reaction temperatures. Ishihara and co-workers<sup>16</sup> tested the effect of the solvent on HDS of BT. They have investigated different solvents under deep HDS conditions over CoMo/  $\gamma$ -Al<sub>2</sub>O<sub>3</sub> catalyst. The extent of conversion of BT into EB at different solvents was reported by them as follows: toluene > decalin > n-pentadecane > 1-methylnaphthalene.

## Chapter 3: Raman spectroscopy-Basic principles

In this chapter, the theoretical background of Raman spectroscopy is presented. The treatment begins with an introduction to the nature of light and how it propagates; then, a brief discussion about the derivation of the number of molecular vibration is introduced; afterwards, a detailed description of Raman effect and its physical mechanism is explained. The main differences between the Raman scattering process and the IR absorption process, along with a brief description of IR process are also presented. After that, the basis of quantitation analysis using Raman spectroscopy is provided. The last section in this chapter presents the depolarization ratio and highlights the importance of depolarization measurements in Raman spectroscopy.

### 3.1 Light

Light, from classical point of view, is considered as sinusoidal waves of oscillating electrical and magnetic fields that are orthogonal to each other. In vibrational spectroscopy only the electric field is considered, while the magnetic field is ignored. The wavy nature of plain polarized light is pictured in figure (3.1). In the figure, the light propagates in the z-direction while the electric field (E) oscillates in the x-z plane and the magnetic field (H) is perpendicular to the electric field and oscillates in the y-z plane. The distance between two successive valleys in the wave train is the wavelength ( $\lambda$ ).

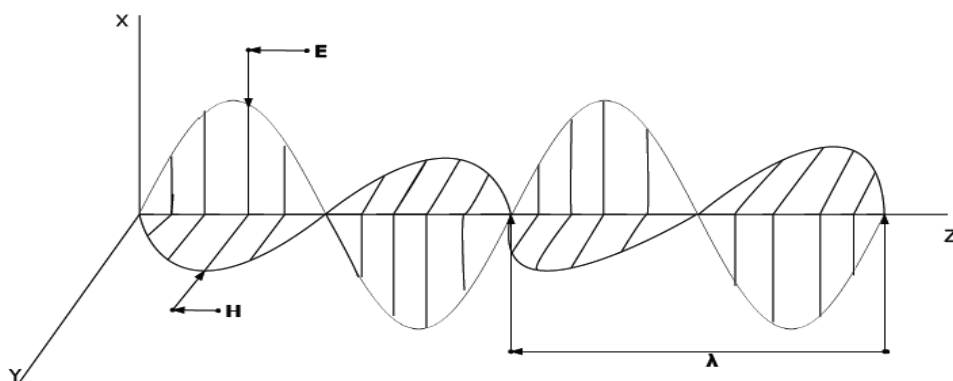


Figure 3.1: Schematic of plain polarized light

The wavenumber ( $\bar{\nu}$ ) in  $\text{cm}^{-1}$  is the measuring unit of vibrational spectroscopy; the wavenumber refers to the number of waves passing a unit length of 1 cm; the wavenumber is related to the wavelength by equation (3.1); the relation between wavenumber and frequency of light ( $\nu$ ) is clear in equation (3.2) where ( $c$ ) is the speed of light in the medium:

$$\bar{\nu} = 1/\lambda \quad \text{Equation (3.1)}$$

$$\bar{\nu} = \nu/c \quad \text{Equation (3.2)}$$

The wavenumber is not an energy unit but it is linked to the energy of the radiation ( $E$ ) by equation (3.3).

$$E = hc (\bar{\nu}) \quad \text{Equation (3.3)}$$

Whereas ( $h$ ) is Planck's constant.

Light can be polarized or unpolarized. Polarization of light refers to the projection at which the electric field of light traces out while it propagates; when the projection is linear, the light is called plain-polarized or linearly-polarized as pictured in figure (3.1). The light is called plain polarized or linearly-polarized because it oscillates in specific plane and the projection of that plane is line; the other states of polarization are circular and elliptical when the light traces out a circle or an ellipse respectively. Laser is an example of polarized light; however, the unpolarized light such as the light of the sun or electric bulb, could be polarized by the means of polarizer, which is an optical element that allows a light of specific polarization state to pass and rejects the other polarization states.

### 3.2 Degrees Of Freedom For Molecular Vibrations

Vibrational spectroscopy is the discipline of science that studies molecular vibrations to determine molecular structure. The term “molecular vibration” refers to the motion of a molecule's nuclei relative to each other<sup>17</sup>; it is neither a translational motion because it

doesn't involve a net change in linear momentum nor a rotational motion because it doesn't involve a net change in angular momentum<sup>17</sup>.

The terms fundamental vibration, normal vibration or normal mode of vibration are all used to describe the molecular vibration<sup>17</sup>. As a rule of thumb, the number of fundamental vibrations of a molecule with N number of atoms is  $3N-6$  for non-linear molecules and  $3N-5$  for linear molecules<sup>5,17,18</sup>. Each atom in the Cartesian space has 3 degrees of freedom (x, y and z). For a molecule with N number of atoms, there are  $3N$  degrees of freedom. In the case of a non-linear molecule, 3 translational degrees are required to specify the position of the molecule in the space and 3 degrees is for rotational motion while 2 degrees of freedom is required for rotation in case of linear molecule<sup>17,18</sup>; the other  $3N-6$  (non-linear) or  $3N-5$  (linear) degrees specify the vibrational motion which either involve changing the internuclear distance between atoms or changing the angle between atoms. The actual normal mode of vibrations could be more or less than the  $3N-6$  rule. Reasons for seeing more modes of vibration include sum tones and over tones<sup>17,18</sup>; however, less modes of vibration could be observed due to several reasons such weakness of the bands which make them undetectable, bands could be outside the instrumental detection range and the most important reason is the degeneracy<sup>17</sup>; degeneracy refers to the presence of coincident bands at the same or very close frequencies; the degenerate bands arise due to molecular symmetry, the higher the symmetry, the more the degeneracy and the less the vibrational bands. Mathematically, the symmetry concepts in group theory are applied on vibrational spectroscopy to predict which bands are Raman or IR active<sup>17,18</sup>; the discussion of group theory is beyond the scope of this work.

### **3.3 Raman Scattering Process**

Classically, the Raman effect is a result of interactions between the oscillating electric field of plain-polarized laser light and the molecules. The electric field of the incident laser could be thought as an oscillating electrical capacitor that alternates its charges periodically in a frequency equal to the frequency of the light. Molecules are significantly smaller than the wavelength of this incident light, which effectively makes the molecules

bathed in an oscillating electrical field. These oscillations distort the electronic density around the chemical bonds of the molecules, causing temporary induced dipole moments which leads to bond vibrations. The ease at which the electronic density of a chemical bond is distorted is called polarizability; the greater the change in polarizability, the greater the induced dipole moment and the stronger the vibration<sup>17</sup>. Therefore, the selection rule for vibration to be Raman active is the change in polarizability.

The Raman effect is small or forbidden for polar bonds of permanent dipole moment because the electrons are held firmly by the electronegativity of atoms; however, these bonds are strongly IR active. On the other hand, bonds and atoms with high concentration of loosely held electrons, such as non-polar bonds, are strongly Raman active because the electron clouds are easily distorted by the external electric field. Notably, these bonds are weak or forbidden in IR. Figure (3.2) shows the temporary dipole moment of a homo-nuclear diatomic molecule induced by the external electric field of the incident light.

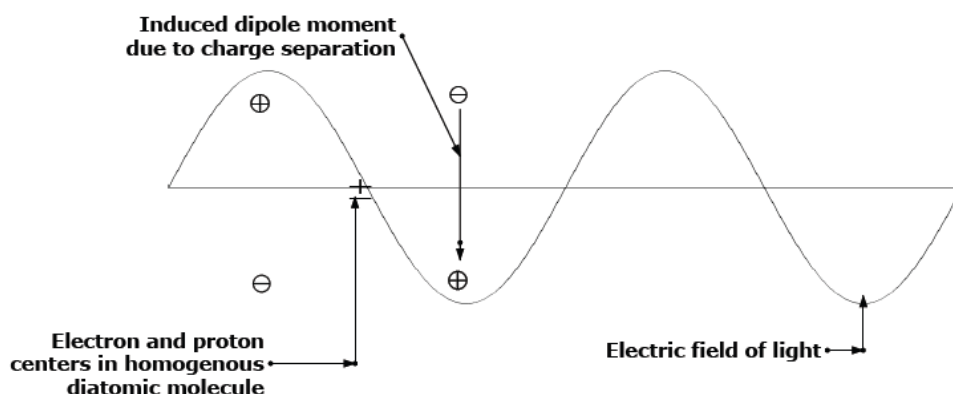


Figure 3.2: Temporary dipole moment of a homo-nuclear diatomic molecule induced by the external electric field of incident light

From the quantum mechanics point of view, the Raman effect is pictured as an inelastic scattering between photons and molecules with the following assumptions: light is considered as massless discrete energy units called photons; when monochromatic incident light of frequency  $\nu_0$  interacts with a molecule at stable ground state the electron density of molecule momentarily absorbs these photons and are excited to non-stable

virtual state which is not a real energy state; spontaneously the electron density drops back to lower stable state with emission of photons. If the emitted photons have the same frequency,  $\nu_0$ , as the incident photons, the scattering is elastic in nature and is called Rayleigh scattering. This type of scattering does not include energy transfer to the molecule and consequently is not associated with changes in bond vibration; it only results in changes in the direction of the light. On the other hand, if the emitted photons have a different frequency than the incident photons,  $\nu_{obs}$ , the scattering is inelastic in nature and is called Raman scattering. This type of scattering involves energy transfer to the molecule and consequently results in changes to the bonds vibration at frequency  $\nu_{vib}$ . Only a very tiny fraction of the total number of scattered photons will have a different frequency than the incident light. As a result, Rayleigh scattering is an order of magnitude stronger than Raman scattering. The vibrational energy of Raman modes are exactly equal to the energy difference between the vibrational spacing that are involved in IR absorption processes. Thus, Raman spectroscopy offers a tool to study the IR-like vibrations using incident light in UV, visible and near-IR ranges. In order to observe Raman scattering, the stronger Rayleigh scattered photons must be ignored, usually through filtering. The elastic and inelastic scattering models are represented in figure (3.3).

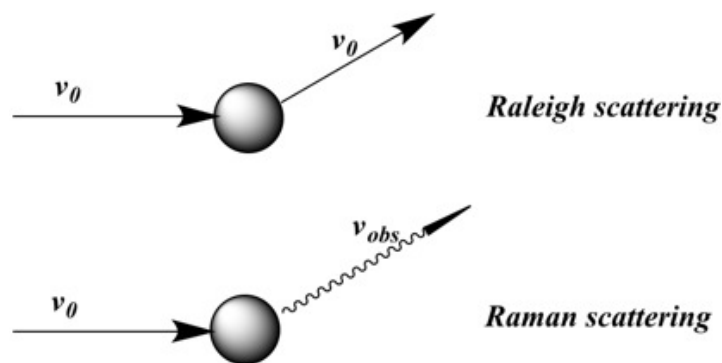


Figure 3.3: Collision model of light scattering

Raman shifts are categorized into two types: Stokes bands and anti-stokes bands. Both of these bands are identical in terms of the wavenumber but differ in the initial state of excitation. Stokes bands are more dominant and occur via collisions of photons of energy

$h\nu_0$  with molecule at a ground vibrational state (defined at  $v = 0$ ). Subsequently, the molecule will vibrate at a frequency  $\nu_{\text{vib}}$  and photons will be emitted or scattered with frequency  $\nu_{\text{obs}}$ , which is less than the frequency of the incident photons. For Stokes Raman shifts; the incident photons frequency,  $\nu_0$ , the scattered photons frequency,  $\nu_{\text{obs}}$ , and the Stokes Raman vibrational frequency,  $\nu_{\text{vib}}$ , of the excited molecule are related by equation (3.4):

$$\nu_{\text{vib}} = \nu_0 - \nu_{\text{obs}} \quad \text{Equation (3.4)}$$

The less dominant anti-Stokes Raman bands occur via collisions of photons of frequency  $\nu_0$  with molecules at the 1<sup>st</sup> excited vibrational state (at  $v = 1$ ). In this case, the emitted photons will gain energy and scatter photons at a frequency higher than the incident light frequency. The schematic in figure (3.4) shows the energy level involved in the scattering and equation (3.5) describes the relation between the incident photons frequency, scattered photons frequency and the anti-Stokes Raman frequency of the molecule.

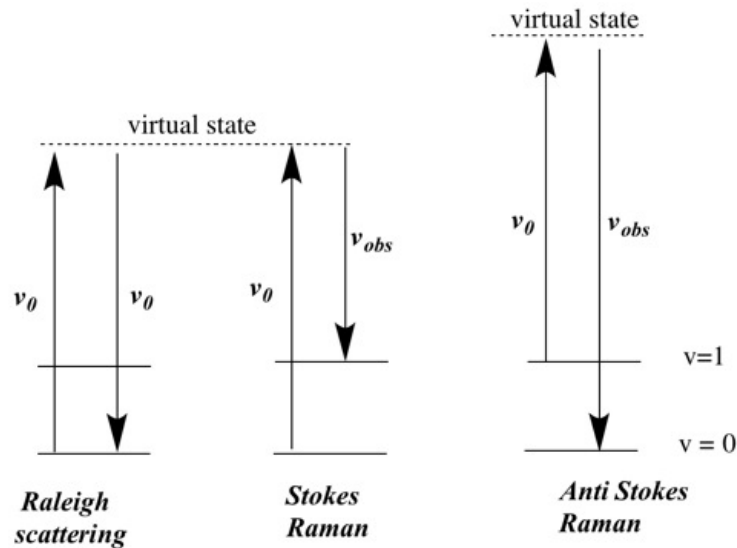


Figure 3.4: Schematic for energy levels involved in scattering.

Boltzmann's law describes the ratio between Stokes and anti Stokes Raman shifts at thermal equilibrium. Because most molecules reside at the ground vibrational state at

room temperature, the intensity of the Stokes Raman lines are much more intense than the anti-Stokes<sup>18</sup> lines.

The Raman spectrum is called Raman shift because it describes the shift in wavelengths between the incident photons and the scattered photons; the associated wavenumber in  $\text{cm}^{-1}$  for Stoke Raman shift is calculated by equation (3.6).

$$\Delta \bar{\nu} = \left( \frac{1}{\lambda_0} - \frac{1}{\lambda_s} \right) 10^{-7} \quad \text{Equation (3.6)}$$

Where  $\Delta \bar{\nu}$  is the Raman shift in  $\text{cm}^{-1}$ ,  $\lambda_0$  is the wavelength of the incident light in nanometers and  $\lambda_s$  is the wavelength of scattered light in nanometers.

### 3.4 IR Spectroscopy Vs. Raman Spectroscopy

Both the Raman effect and IR absorption processes result in the same kind of vibrational frequencies. These frequencies are similar because the molecular energy spacing involved in both processes are the same, namely the ground vibrational state and the 1<sup>st</sup> excited vibrational state. Both processes are complementary and each one supplements the other. Even though Raman and IR processes arise from totally different mechanisms, they result in complimentary spectra where vibrational modes that are intense in Raman are weak or inactive in IR and vice versa.

IR vibrational modes arise when the resonance absorption condition is satisfied; in other words, the chemical bond will absorb light and vibrate when the frequency of the incident light matches the natural frequency of molecular vibration. In terms of quantum mechanics terminology, chemical bonds will absorb incident photons when the energy of these photons is equal to the difference in the energy between the two molecular states involved in vibration. This effect is called Bohr resonance and it is the first selection rule for a bond vibration to be IR active. On the other hand, the Raman effect is an off-resonance interaction between the electrical field of the light and a molecule's electronic density; the Raman effect is much closer to be emission process than an absorption process.

The second selection rule for IR spectroscopy is that the vibration must change the dipole moment of the chemical bond. The dipole moment in short describes the separation between electric charges in the molecule. The dipole moment is determined by molecular



orbital calculations and could be approximately estimated by the comparison of electronegativities of atoms. The bond will vibrate if its interaction with light can produce a change in dipole moment; the greater the change in the dipole moment, the more intense the IR band. Generally, molecules with permanent dipole moment such as hydrochloric acid HCl are strongly IR active because the electric field of the light acts differently on the two ends of the molecule, which greatly change the dipole moment. On the other hand, molecules with symmetry such as hydrogen H<sub>2</sub> are IR inactive since the symmetry does not allow charges separation and hence no change in the dipole moment. Furthermore, the change in dipole moment and the change in polarizability are contradictory mechanisms; when one of them is strong the other is weak or forbidden and vice versa. Thus, asymmetric chemical structures and polar bonds such as the chemical functional groups, which have strong dipole moment, are easily detected by IR technique, while the symmetric chemical structures and non-polar bonds such as the molecular framework, which have strong polarizability, are easily detected by Raman technique.

In IR spectroscopy, the incident light is multi-chromatic that includes all the IR frequencies. A specific frequency will be absorbed when it matches with any molecular vibrational frequency; the greater the absorption, the stronger the IR band. The IR spectrum is plotted with absorption intensity on the vertical axes and the wavenumber on the horizontal axes. On the other hand, monochromatic light is used as incident light in Raman spectroscopy. Raman vibrational mode will appear when the incident light causes a change in bond polarizability. The transmission intensity of Raman spectrum is plotted on the vertical axis while the shift in the wavenumber is plotted on the horizontal axis.

Carbon dioxide molecule, CO<sub>2</sub>, is a good example to show the difference between the IR and Raman selection rules and to show the effect of symmetry on the vibrational modes. Although CO<sub>2</sub> has no permanent dipole moment due to its symmetry, but the molecule exhibits two intense IR bands at 2349 cm<sup>-1</sup> and at 667 cm<sup>-1</sup> and exhibit one Raman active band at 1337 cm<sup>-1</sup>. Figure (3.5) depicts the effect of electrical capacitor on CO<sub>2</sub>. Recalling that the electric field of light works as alternate electrical capacitor. The CO<sub>2</sub> molecule consists of two identical oscillators C=O sharing carbon as a central atom; the two oscillators could stretch simultaneously by the attraction to the capacitor charges, this is mode 1 which is symmetric stretching mode which is Raman active because it involves a

change in polarizability; however, this mode is IR inactive because the net change in dipole moment is canceled out due to the symmetry in stretching. In mode 2 that is located at  $2349\text{ cm}^{-1}$ , when one oscillator stretches towards the capacitor, the stretching of the carbon atom compresses the oxygen atom in the other oscillator and a symmetric stretching mode arises. This mode is IR active but Raman inactive because it only includes a change in dipole moment. Mode 3 is the bending mode that is located at  $667\text{ cm}^{-1}$ . When the lighter carbon atom moves right due to the attraction to the capacitor, the angle between the carbon and the oxygen atoms will change which changes the dipole moment but not the polarizability; upon alternating the capacitor charges, the carbon atom will pass the equilibrium point and move to the left. This bending mode is IR active but Raman inactive.

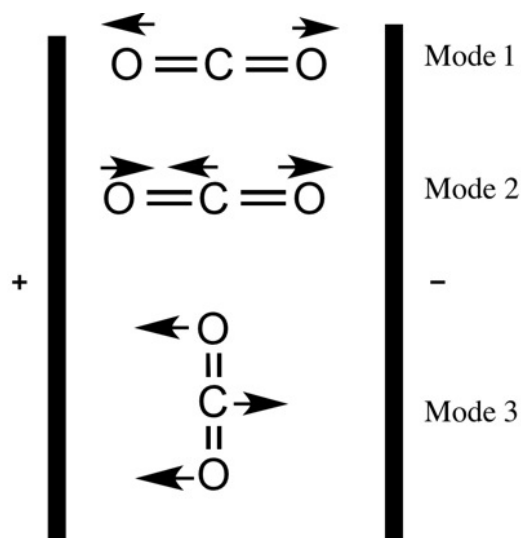


Figure 3.5: Modes of vibration for CO<sub>2</sub>.

Experimentally, the Raman technique moved out of the shadow of IR technique during 1990s<sup>19</sup>. The introduction of diode lasers, fiber optics, high sensitivity detectors and fast personal computers have revolutionized the Raman spectroscopy<sup>6,8,19</sup>. The following points summarize the main advantages for Raman technique over IR spectroscopy:

- 1- The Raman test could save significant cost by requiring no sample preparations<sup>8,19</sup>; sample preparations may include grinding, dissolution, separation or other steps. Grinding could change the hydration state, the polymorphism state

- or other solid states<sup>19</sup>. Thus, this advantage is important when looking for active ingredients specially for quality control purposes<sup>19</sup>.
- 2- Raman spectra could be obtained for colorless sample sealed in a container using laser in the visible range<sup>8</sup>; therefore, the Raman spectra for corrosive, air sensitive, or hygroscopic samples could be measured while the sample is sealed<sup>8</sup>.
  - 3- The fiber optics interfaces allow acquiring Raman spectra for remote processes which enables real time monitoring of severe chemical environments and has given the Raman spectroscopy proven advantage over IR spectroscopy<sup>8</sup>.
  - 4- Water is a weak Raman scatterer and strong IR absorber. This gives Raman technique particular importance for analyzing aqueous solutions<sup>8,19</sup>.
  - 5- The depolarization ratio measurements which could be achieved in Raman spectroscopy provide information about the vibrational symmetry and molecular orientation; however, IR spectroscopy doesn't provide such measurements<sup>5</sup>.
  - 6- Raman analysis is short in time and requires minimum training.

### 3.5 Intensity of Raman signal

The following relation describes the absolute intensity of Raman signal:

$$I_R \propto \nu^4 I_0 N \left( \frac{\partial \alpha}{\partial Q} \right)$$

Where  $I_R$  is the Raman intensity,  $\nu$  is the frequency of incident light,  $I_0$  is the intensity of the incident light,  $N$  is the number of scattered molecules,  $\partial \alpha$  is the change in polarizability and  $\partial Q$  is the change in vibrational amplitude<sup>18</sup>. The term  $(\partial \alpha / \partial Q)$  is the Raman cross section and it is constant for particular material at particular wavelength<sup>20</sup>. Since the number of scattered molecules  $N$  is related to the concentration of that molecule in the sample, the Raman signal is concentration dependent and consequently Raman spectroscopy could be used for quantitation. Unfortunately, some of the parameters mentioned in the above relation can't be determined that makes it extremely difficult to use the absolute Raman intensity relation for quantitation purposes<sup>8</sup>; therefore, empirical methods are developed to measure the concentration of specific component in the sample.

Basically, the spectroscopic quantitative analysis relies on fitting a calibration curve between the signal intensity produced by the analyte and the analyte concentration. In case of Raman, the signal intensity could be either the peak height or the peak area of specific band. The selection of appropriate band is the basis of accurate quantitative analysis; for example for binary mixture, the strongest band that is unique for each component is selected as basis of quantitation.

In order to develop a calibration curve, a series of exactly measured standards of different concentration of the two-component mixture are prepared; these standards should cover the concentration range under consideration; afterwards, the spectra of these standards are acquired and the intensity of the selected band are plotted against the analyte concentration. Most of the time the calibration curve is not linear and this is expected due to non-linearity factors such as overlapping of bands and molecular interaction<sup>20</sup>. One way to deal with non-linearity is to fit an empirical polynomial curve, which is usually the case with instrumental software. However, a semi-empirical equation based on linear fractional transformation could be used to easily deal with non-linear calibration curve in a manner similar to developing a linear fit<sup>20</sup>.

The semi-empirical fractional transformation equation takes into account the non-linearity nature of Raman signal by considering the interaction between molecules. The intensity of each component is a function of the concentration of the two components as shown in equations (3.7) and (3.8)<sup>20</sup>:

$$R_A = K_{1A} C_A + K_{1B} C_B \quad \text{Equation (3.7)}$$

$$R_B = K_{2A} C_A + K_{2B} C_B \quad \text{Equation (3.8)}$$

Where  $R_A$  and  $R_B$  are the Raman intensities of component A and component B respectively;  $C_A$  and  $C_B$  are the concentration of component A and component B respectively;  $K_{1A}$ ,  $K_{1B}$ ,  $K_{2A}$  and  $K_{2B}$  are constants. By addition and rearrangement of the above equations, the mole fraction of A could be written as<sup>20</sup>:

$$\text{Mole fraction of } A = \frac{C_A}{C_A+C_B} = \frac{aR_A+bR_B}{(R_A+dR_B)} \quad \text{Equation (3.9)}$$

Constants a, b and d are determined empirically.

### 3.6 Depolarization Ratio

In figure (3.6) a molecule centered at the point of origin is irradiated by plain-polarized laser propagates in the Y direction and oscillate in the YZ plane (colored in black). The scattered light is collected in X direction (90° geometry). When the molecule shows total symmetric vibration, all the scattered light will have the same plain of polarization namely YZ plain; the scattered light is called p-polarized or parallel component. On the other hand, when the molecule exhibits non-total symmetric vibration, part of the scattered light will be polarized in XY plain which is a plain perpendicular to the plain of incidence<sup>5</sup>. This is called the s-polarized or perpendicular component (colored in green).

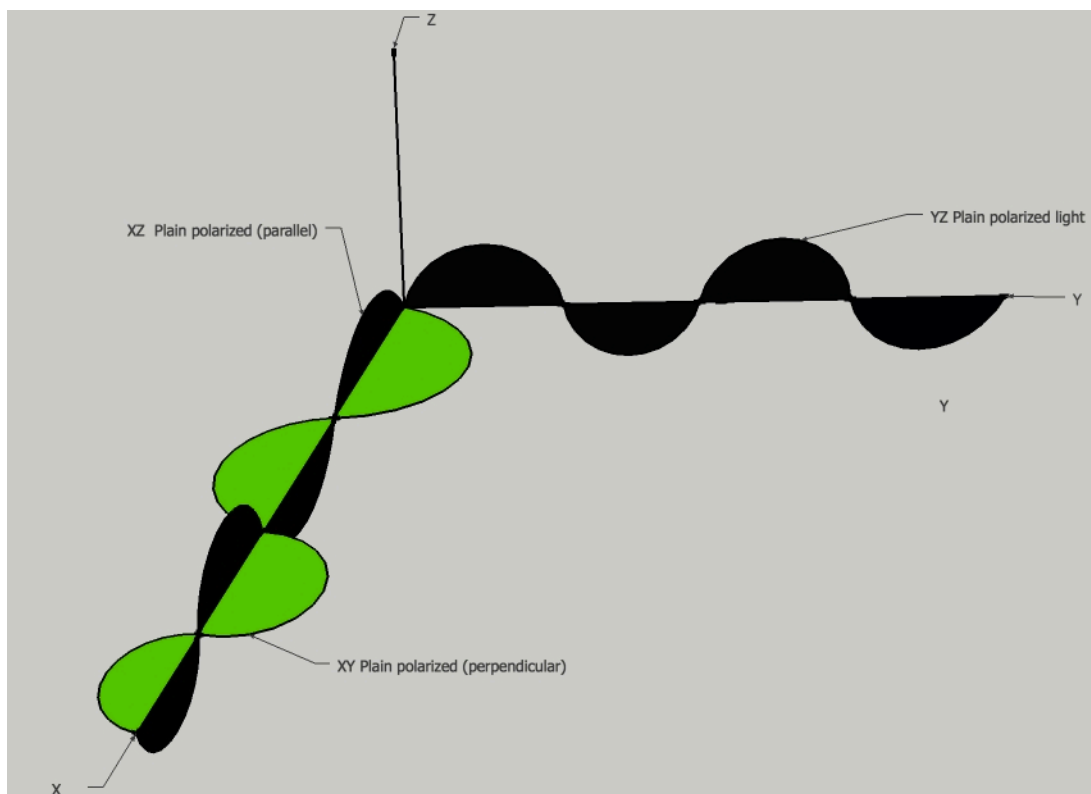


Figure 3.6: schematic of parallel (black) and perpendicular (green) components of scattered light.

The ratio of the intensity of perpendicular component to the intensity of parallel component is called depolarization ratio ( $\rho_p$ )<sup>1,5</sup>. Equation (3.10) shows how to calculate the depolarization ratio:

$$\rho_p = I_{\perp} / I_{\parallel} \quad \text{Equation (3.10)}$$

Whereas  $I_{\perp}$  denotes for the intensity of perpendicular component and  $I_{\parallel}$  denotes for the intensity of parallel component.

In Raman spectroscopy the depolarization ratio measurement is important because it gives information about the symmetry of specific vibration<sup>5</sup>. When the vibration is totally symmetric, the oscillation of the induced dipole moment will be equal in all directions and the polarizability ellipsoid will be spherical. This vibration is called polarized and will scatter only parallel component of light ( $I_{\perp} = 0$ )<sup>5</sup>. However, when the vibration is non-totally symmetric, the induced dipole moment will be directed towards the axis that have greatest polarizability; consequently, the polarizability ellipsoid will not be spherical and will be randomly directed because molecules in liquid and solution are randomly directed<sup>5</sup>. This kind of vibration is called depolarized and the perpendicular component will be greater than zero. Numerically, when the depolarization ratio is  $0 \leq \rho_p < 0.75$ , then the band is totally symmetric (polarized). On the other hand, when the  $\rho_p = 0.75$ , then the band is non-totally symmetric (depolarized)<sup>5</sup>.

## Chapter 4: Instrumentation And System Development

### 4.1 In-Situ Raman Hot Stage Reactor: The Basic Items

A typical Raman spectroscopy system consist of four basic elements<sup>8,20</sup>:

- 1- Laser source
- 2- Sample illumination and collection optics
- 3- Spectra analyzer
- 4- Detection system

The typical arrangement of these elements is depicted in Figure 4.1.

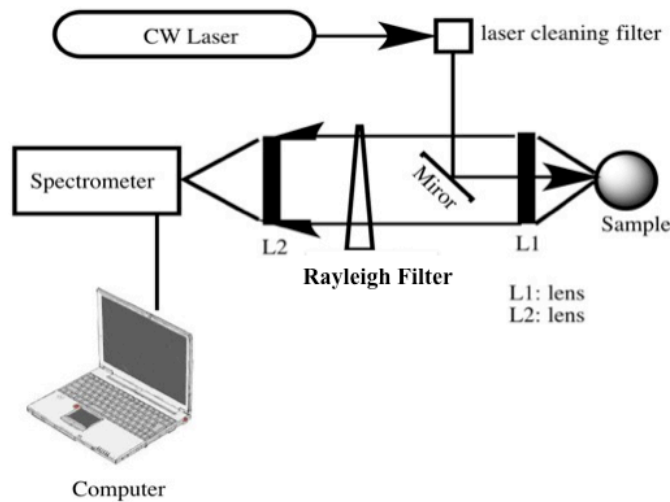


Figure 4.1: Typical arrangement of Raman system.

Raman spectroscopy usually uses a Continuous Wave (CW) laser source that emits a specific wavelength light with a constant output power<sup>8</sup>; the sample illumination optics are configured to remove unwanted plasma lines from the laser light and adjust its polarization. Additionally, the illumination optics focus the laser beam on the sample while the collection optics collect the backscattered light and filters out the original laser

frequency. The resulting shifted laser frequencies are passed to the spectral analyzer or wavelength selector, where the backscattered light is analyzed to different frequencies and guided to the detector.

To achieve the goal of conducting *in-situ* spectral measurements for reactive system, it is required to continuously deliver the laser light to a mini-reactor (hot stage reactor) and simultaneously collect the backscattered light from the reactor that operates at high temperature and sometimes high-pressure. The custom built hot stage reactor that had been developed by Bagheri et al.<sup>1</sup>, has been adapted for use in this project; this reactor is equipped with a transparent c-axis oriented sapphire window that allows polarized light transmission into the reactor and is able to handle severe conditions of temperature and pressure.

The *in-situ* Raman hot stage reactor that has been implemented in this project consists of the following items:

- 1- Fiber coupled Raman laser module.
- 2- Custom built hot stage reactor.
- 3- Spectrometer for Raman application.
- 4- Sample illumination and collection system that includes the following:
  - a- Polarization probe with separate parallel and perpendicular light channels.
  - b- Excitation and collection fiber optics.
  - c- Three-dimensional motorized stage.
- 5- Light tight enclosure.



Figure 4.2 shows the *in-situ* Raman hot stage reactor that has been developed to investigate *in-situ* mesophase formation.

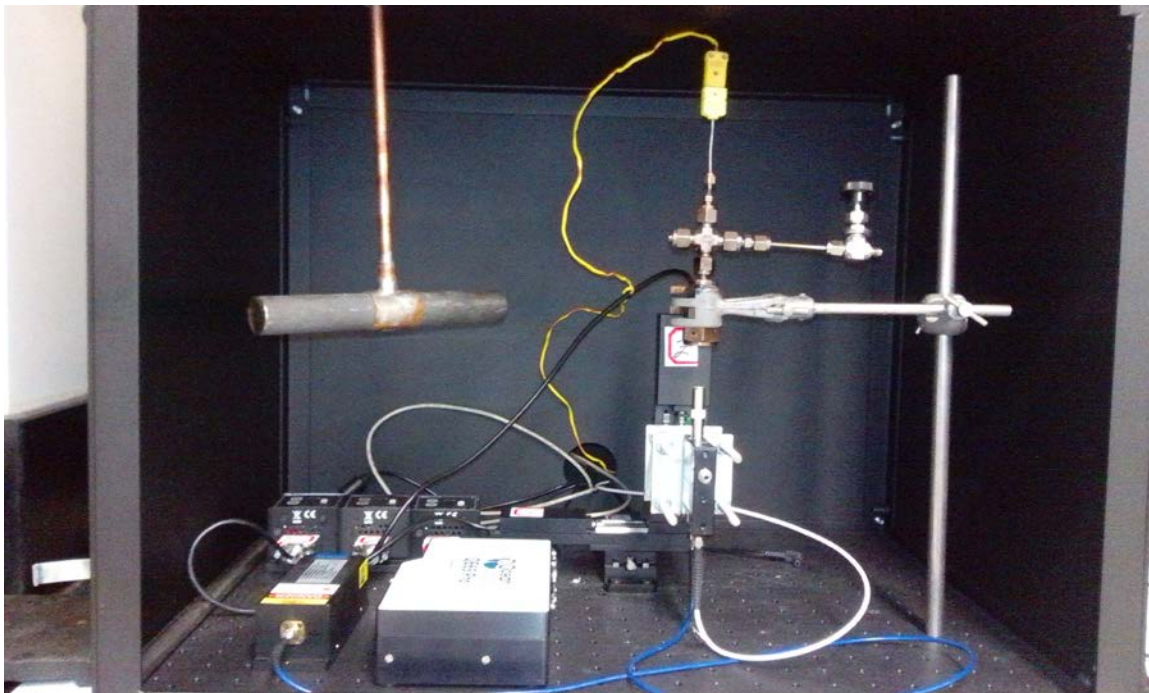


Figure 4.2: In-situ Raman hot stage reactor.

## 4.2 System Safety

Safety is the first, and the most important, priority that should be considered when dealing with practical systems either in industrial or academic fields; the working environment must be safe for everyone in the laboratory. Without the necessary safety controls, the *in-situ* Raman hot stage reactor system could potentially cause hazards due to the well known hazards associated with lasers and due to the relatively high pressure of the micro-reactor system. The laser hazard specifically comes from working with a class 3b laser. Class 3b lasers are regulated in Alberta by the Radiation Protection Regulation; based on these regulations, all class 3b lasers must be registered before being used. These safety regulations have been adopted from American National Standards for Safe Use of Lasers, ANSI Z136.1-2000<sup>21</sup>. University of Alberta is an Authorized Radiation Health Administrative Organization that can register class 3b lasers owned by the University<sup>21</sup>; The office of Environmental Health and Safety (EHS) at the University of Alberta is an Authorized Radiation Protection Agency (ARPA) which is a legal provincial authority that can inspect and engage all services related to class 3b lasers belonging to the University<sup>21</sup>.

Lasers are considered hazardous if the beam irradiance ( $\text{Wcm}^{-2}$ ) and radiant exposure ( $\text{J cm}^{-2}$ ) exceed the maximum permissible exposure (MPE). The specific class 3b laser that is used in this work can cause eye and skin damage but not photochemical damage. In general, the eye damage is more hazardous to researchers than the skin damage because the maximum permissible exposure of the eye is much lower than that of the skin<sup>21</sup>. The lower MPE for the eye is due to the deep penetration and absorption of the laser light, which causes a retina hazard in case of 785nm laser, and the optical gain of the eye lens that focuses the light on the retina by 5 orders of magnitude. Both direct beams and specular reflected beams are serious eye hazards while the diffusive reflected beam is much less hazardous<sup>21</sup>. In the case of near-IR lasers, e.g. a 785nm laser, only the thermal effect on the skin is the potential hazard. Thermal effects occur when the rate of laser absorption by the skin is greater than the conduction rate by which the surrounding tissues safely dissipate the heat from the exposed tissue. In the case of a 785nm laser, only the direct beam and the specular reflected beam can cause skin effects but not the

diffusive reflected beam; the thermal effect ranges from 1<sup>st</sup> degree burn up to 3<sup>rd</sup> degree burn<sup>21</sup>.

The nominal hazardous zone (NHZ) is the space where the direct, reflected or scattered laser beams exceed the MPE limit of a given laser and within which people should wear the protective equipment<sup>21</sup>; the evaluation of the NHZ some times include complex calculations to determine the irradiance and radiant exposure for all potential laser beams. The laser safety officer should do the evaluation of the nominal hazardous zone, and this evaluation is beyond the scope of this project. A set of control measures have been adopted and another set of control measures will be implemented soon to ensure that the level of exposure to laser radiation is below the MPE limits of eye and skin; also some of the control measures are intended to eliminate the non-beam hazards. The control measures under consideration are divided into three categories: engineering control measures, protective equipment and administrative measures. The following control measures are required for this project:

#### **A. Engineering Control Measures**

- 1- The excitation laser and the scattered laser have been transferred via fiber optics; this will significantly minimize the accidental exposure to direct, reflected or scattered laser.
- 2- The system elements have been fixed to an optical table; this keeps the laser in the intended path and helps in laser alignment.
- 3- The whole system has been placed inside a custom built enclosure to minimize the nominal hazardous zone; the enclosure is made of 3 mm thick aluminum sheets which can resist prolonged laser exposure due to high laser damage threshold for aluminum; the enclosure has been coated with matt black color in order to absorb most of the laser light energy; also, the surface of the enclosure is rough to ensure that the irregularities in the surface are larger than the laser wavelength and this causes diffusive reflection for the portion of laser beam that is not absorbed. Finally, an electric switch should be installed on the enclosure lead to confirm shutting off the laser when the enclosure is opened and this will eliminate any laser hazard.

- 4- A warning sign, which has been designed according to ANSI Z136.1-2000 standards, is activated when the laser is in operation to warn people of the laser hazard in the lab, to indicate the type and the class of the laser being used, and to provide instructions about using protective equipment<sup>21</sup>.
- 5- To minimize the laser hazard during alignment of the laser on the reactor, the alignment is done using an accurate computer controlled motorized stage while the enclosure is closed; the optimum alignment is confirmed by scanning the reactor surface until the maximum spectra is obtained.
- 6- CSA approved heating tape have been used as a heating source; this tape is grounded to prevent any electric charges build up.

## **B. Protective Equipment Measures**

- 1- The laser goggles, the lab coat and the gloves have been worn when working within the enclosure while the laser is in operation.
- 2- The laser goggles are regularly cleaned and inspected for any cracking, coat damage or discoloration; also, the goggles should not be subjected to direct laser for more than 10 seconds to avoid filter damage (threshold damage). Finally, since multi-laser environments are presence in the lab, it is recommended to have color-coding on the laser goggles to avoid any possibility of eye damage.

## **C. Administrative Control Measures**

- 1- Only persons with safety laser training are allowed to operate this system; the training is essential to protect people from any potential laser hazards; the people who are running this system have got their training in the office of Environmental Health and Safety (EHS) at University of Alberta.
- 2- As mentioned earlier, only trained people are allowed to run this system; and so, the system should be protected from unauthorized use by untrained person; this protection could be achieved by using the remote control feature in the laser module; the laser module could be connected and controlled by the computer

which is protected by a password owned only by the trained people who are running the system. On the other hand, a lock should be installed to protect the enclosure.

- 3- Standard operating procedures have been written to show step-by-step instructions to operate the system safely.
- 4- The reactor is leak tested to double the working pressure to guarantee the confinement of the laser generated air contaminates inside the reactor and also to prevent failure of the reactor due to high pressure operation. Laser generated air contaminates (LGAC) can be generated due to vaporizing effect of the laser on the target material; these contaminates could be hazardous and the measure controls should eliminate this risk.
- 5- Class 3b lasers are a possible fire hazard in the presence of flammable materials; and so, laser should not be directed at any combustible material. The reactor usually contains potentially combustible material such as hydrogen and organic solvent; and so to mitigate the risk of combustion, the reactor is purged several times by nitrogen to remove any oxygen prior to each experiment, also the reactor has been leak tested at double working pressure to be sure that there was no leak of hydrogen or other combustible materials.
- 6- A gas detector is used to check any hydrogen leak from the reactor in order to eliminate any fire hazards.

## 4.3 System Design

### 4.3.1 Hot Stage Reactor Design

#### 4.3.1.1 Overview

Many researchers have reported using hot stage reactors coupled with optical polarized microscopes to study *in-situ* carbonaceous mesophase formation<sup>1</sup>; this technique allows on-line visual observation of the sample subjected to heating; it is also capable of determining the phase type, phase transition temperature and the growth of the mesophase with increasing temperature<sup>1</sup>. Bagheri<sup>1</sup> has used a custom built hot stage reactor in his thesis to investigate mesophase formation and the same reactor is adopted in this work; his reactor is a modified version of a previous reactor used by Rahimi et al.<sup>22</sup>. In Rahimi et al. reactor<sup>22</sup>, the sample was placed in aluminum cup that was inserted in the hot stage cell; the hot stage cell was then covered by YAG crystal which works as viewport; the hydrogen was passed over the aluminum cup. The new reactor designed by Bagheri<sup>1</sup> was designed to be mated to an inverted microscope and aimed to overcome the drawbacks of Rahimi et al. reactor<sup>22</sup> which was compatible with upright microscope. Bagheri<sup>1</sup> solved the problem of forced heat convection by the sweeping gas and the natural heat convection through the YAG window by using inverted reactor design which eliminate the space between the reactor window and the sample and allow direct contact between them; also, he has replaced the YAG window with sapphire window which has much better thermal conductivity. On the other hand, the new design by Bagheri<sup>1</sup> doesn't require the aluminum cap to hold the sample, which lead to further decreasing the thermal resistant throughout the reactor. For a complete analysis for the reactor, the reader could refer to Bagheri<sup>1</sup>. The better thermal distribution in the new design eliminates the gas condensation on the window, which was noticed with old reactor; also, the better thermal distribution cancels the temperature gradient in the sample and allows getting better homogenous texture. The introduction of the mixer in the new design suppresses dispersion of the sample to the wall due to the surface tension and improves

the heat transfer which leads eventually to have better homogenous texture<sup>1</sup>. The schematic for the two designs are depicted in Figure (4.3.a) and Figure (4.3.b.)

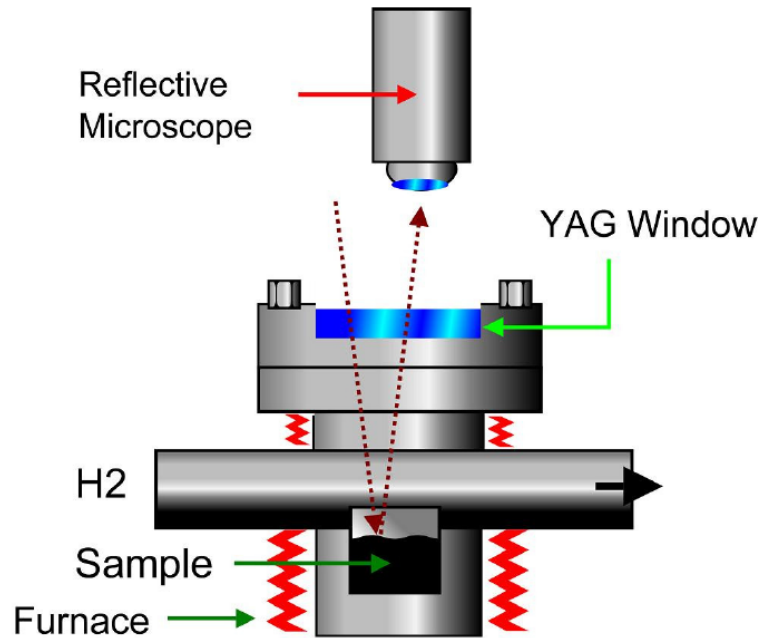


Figure 4.3.a: Hot stage reactor used by Rahimi et al.<sup>22</sup> (Adopted from Bagheri<sup>1</sup>)

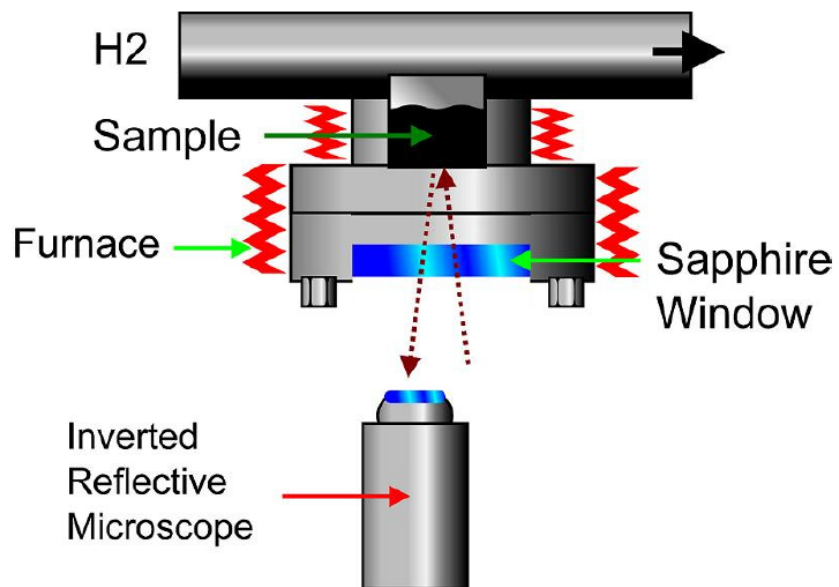


Figure 4.3.b: New hot stage reactor used by Bagheri.<sup>1</sup> (Adopted from Bagheri<sup>1</sup>)

### 4.3.1.2 Reactor Design

In this study, the hot stage reactor designed by Bagheri<sup>1</sup> has been adopted. Figure (4.4.a) and figure (4.4.b) show schematics of the reactor. The reactor body is made of stainless steel Swagelok fittings except the lower part, marked by a square in figure (4.4.a), is made from a stainless steel Parker reducer and nut.

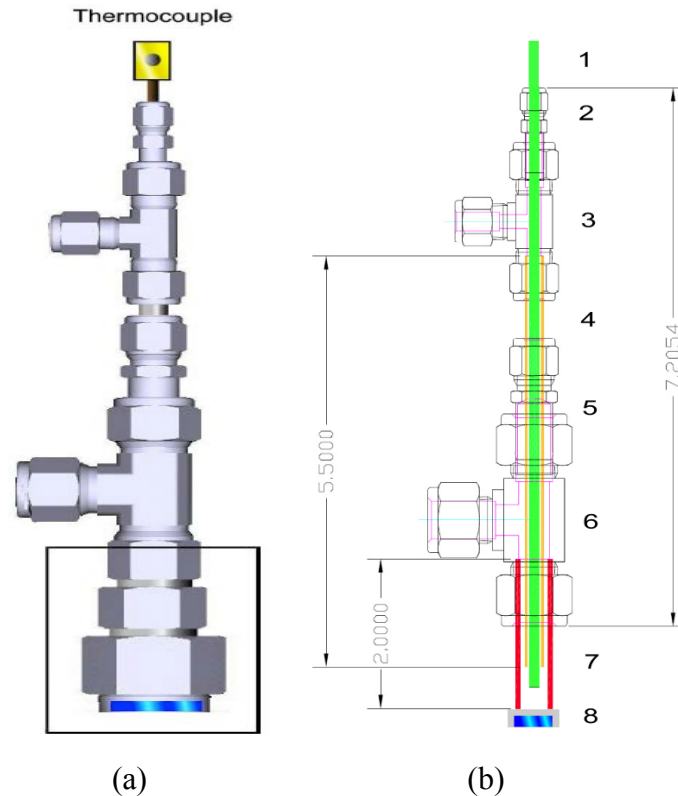


Figure 4.4: (a) Schematic of the reactor with a square surrounding the lower part that consists of Parker fittings. (b) Detailed schematic of the reactor excepting the Parker part: (1) Thermocouple, (2) 1/4''-1/16'' BT reducer, (3) 1/4'' Tee, (4) 1/4'' Tube, (5) 1/2''-1/4'' Reducer, (6) 1/2'' Tee, (7) 1/2'' Tube, (8) Sapphire window. (figure courtesy of Dr. Cedric Laborde-Boutet).

The upper 1/4'' Tee is for connecting the inlet gas while the lower 1/2'' Tee is to connect the outlet gas in case of continuous operation; in the case of batch operation, the lower 1/2'' Tee is usually omitted and the 1/4'' tube is connected to the 1/2'' tube via 1/2''-1/4'' reducer. More detailed information about the lower part of the reactor that is marked by a square in figure (4.4.a) is found in figure (4.5).



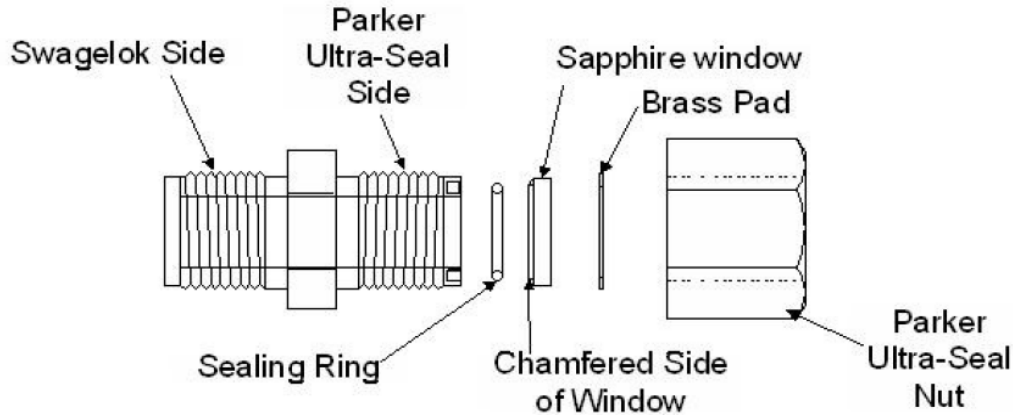


Figure 4.5: Lower part reactor assembly

The Parker 1/2" UltraSeal reducer, part number 8-8QHLZ, has been grooved to fit the O-ring; this reducer comes with 1/2" nut, part number 8 BQ UltraSeal, to seal the sapphire window. Sealing between the sapphire window and the reactor is done via a silver plated O-ring placed on the groove made on the internal edge of the UltraSeal reducer; 0.001" thick brass ring is placed between the window and the nut. Upon heating, the O-ring deforms and seals the reactor.

The sapphire window is optical grade sapphire from Miller Optics Inc. It is single crystal c-plane orientated sapphire to minimize birefringence when illuminated with polarized light; it approximately transmits 85% of light at 785nm wavelength. The window is 0.782" in diameter and 0.158" in thickness. Other narrower and thinner window has been used in this project, it is 0.750" in diameter and 0.125" in thickness; both windows have been tested up to 320°C and 5 MPa

The temperature of the reactor is monitored by 1/16" XL type thermocouple from Omega®; it can measure up to 1335 °C with low thermal drift; it is Nickel-Chrome sheathed which makes it suitable for severe chemical environments. The thermocouple is inserted into the top of the reactor until the lower tip of the thermocouple touches the sapphire window; in the configuration used in this work, the thermocouple has dual functions: it measures the temperature of the reactor and at the same time works as a shaft

for the magnetic mixer; more information about this mixer is presented in the next chapter.

#### 4.3.1.3 Mixing System

The introduction of the stirring inside the hot stage reactor significantly improves the heat transfer and allow the addition of the catalysts for heterogeneous reactions<sup>1</sup>. The mixing is done by custom-made Alnico magnet block; this magnet is passed through the thermocouple that works as a shaft; this small magnet is rotated by coupling it with external strong rotating magnet bar. The magnet block is custom manufactured by Dura Magnetics, Inc. Although the magnetic power of this block is not that much strong, but it the only magnet that can survive without demagnetization at temperature over than 400°C. The magnet block is displayed in figure (4.6). A schematic for the lower part of the reactor with the magnetic stirrer is shown in figure (4.7). In figure (4.1) the external magnet bar that rotates the internal magnet is shown as part of the complete system.

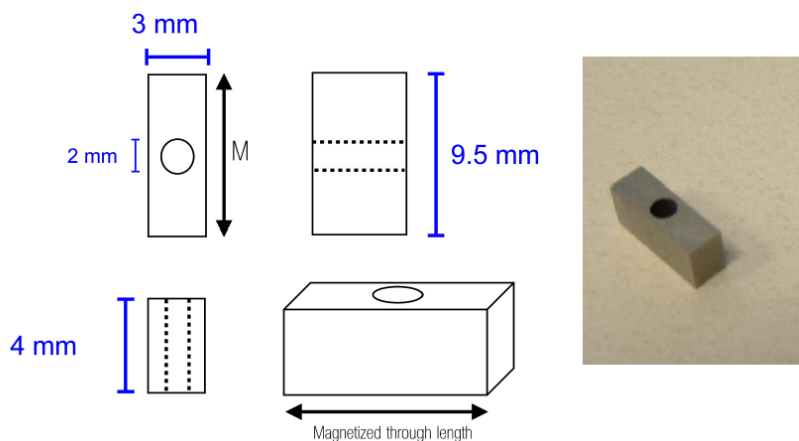


Figure 4.6: Custom-made Alnico magnet block (Adopted from Bagheri<sup>1</sup>).

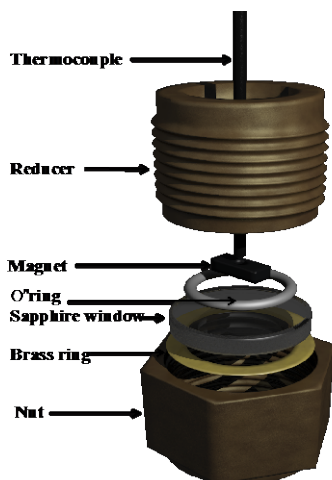


Figure 4.7: Schematic for the lower part of the reactor with the magnetic stirrer (figure courtesy of Dr. Cedric Laborde-Boutet).

#### 4.3.1.4 Heating System

Based on the University policy, electrical heating systems must be approved by the Canadian Standards Association (CSA); the CSA approval demonstrates that the product have been tested and certified according to safety and quality standards applicable in Canada. Thus, a CSA approved heating tape is used as a heating source; this heating tape, model number HT95502, comes from Fisher Scientific; it is a electrically grounded, glass fiber, and flexible heating tape that is suitable for metallic and glass surfaces; this heating tape can operate up to 450 °C, and the control of the temperature is done via external controller. The heating tape is spiraled around the reactor being heated, but due to the irregular external surface of the reactor and to avoid rupture of the tape fiber, some layers of flexible thin steel foam are spiraled around the reactor prior to the wrapping of the heating tape; this steel foam also improve the contact between the heating tape and the reactor. Figures (4.8.a) and (4.8.b) show the wrapping of the steel foam and the heating tape around the reactor. A thick layer of insulation material is rolled up over the heating tape to minimize the heat loss during the heating of the reactor.



(a)

(b)

Figure 4.8: (a) wrapping steel foam around the reactor, (b) wrapping the heating tape over the steel foam.

### 4.3.2 Laser Source

The selection of laser wavelength is a crucial consideration in the development of this system since the type of the detector<sup>20</sup>, the quantum efficiency of the detector<sup>7</sup>, enhancing the signal to noise ratio (S/N), and the employed laser power depend on the selected laser wavelength. Also, undesired fluorescence is commonly encountered with opaque samples, such as in the case of mesophase pitch. Fluorescence can be greatly minimized by the correct choice of laser wavelength.

In this section, the selection criteria of the laser source is presented; it begins with a brief introduction of the laser as an attractive excitation source for Raman spectroscopy, The most popular laser types will also be discussed, specially those in the near-IR region. This discussion will focus on their advantages and disadvantages. Unwanted sample fluorescence will also be discussed as well as possible ways to avoid, or at least to minimize, this effect. Finally, the selected laser source is introduced with the reasoning behind this selection.

As mentioned before, the Raman effect is a weak process and the resultant signal is a weak signal. The introduction of lasers in 1960s as an excitation sources for Raman experiments instead of low-pressure water-cooled mercury arc lamps was the first breakthrough in the development of practical and useful Raman instruments<sup>6</sup>.

Laser beams are collimated, coherent, narrow (highly monochromatic) sources of light that are much more intense than any incoherent light sources<sup>6</sup>. An advantage of laser light sources is that the beam is small in diameter (1-2 mm) and can be easily focused to 0.1 mm by simple lenses. Laser light can be almost completely polarized which makes it perfect for depolarization ratio measurements<sup>8</sup>. These attractive features make lasers the optimum excitation sources for optical instruments including Raman spectroscopy<sup>6</sup>.

There is wide range of lasers, with different wavelengths from the vacuum ultraviolet to the infrared region. A variety of lasers are available that are suitable to Raman spectroscopy<sup>7</sup>; For example, atomic gas lasers like the Argon-ion laser, at 488 nm, are very popular and provide intense power, around 1500mW<sup>8</sup>, in a portable low cost package. The resultant Raman lines are well matched with the optimum sensitivity of photomultiplier tube detector (PMT). The problem with 488 nm lasers is that they are not suitable for use with fluorescent or heat sensitive samples due to excessive heating. The

Helium-Neon laser at 632.8 nm provides low optical power of 5-30mW but it is portable, inexpensive, and the resultant Raman lines match the optimum sensitivity of charged-coupled device (CCD) detectors which make it very popular in Raman spectroscopy<sup>7</sup>. On the other hand, solid state lasers are widely used in Raman community; diode lasers as a solid state lasers can emit a specific wavelength over a wide range of laser lines from visible blue to Infrared spectral region<sup>8</sup>; these diode lasers are inexpensive, small in size, and highly efficient with minimum requirement of power and cooling<sup>8</sup>; the main challenge in using diode lasers is the need to eliminate the drift in the wavelength and to stabilize the emitted frequency<sup>7,8</sup>. These improvements are usually done by precise controlling of the temperature to within  $\pm 0.01^\circ\text{C}$  of the set-point and by installing a grating in the laser cavity<sup>8</sup>.

Nd:YAG laser is an example of solid state diode-pumped laser; it can emits both continuous wave (CW) laser or pulsed laser with optical power up to 10W<sup>8</sup>. Nd:YAG laser emits light near-IR region mainly at 1064nm which is the wavelength for FT-Raman spectroscopy. The introduction of FT-Raman was a major development in Raman measurements because it greatly reduces fluorescence that is encountered with lasers in the visible spectral region which facilitate to get Raman spectra for many fluorescent samples<sup>20</sup>.

The energy of photons in the near-IR region is not normally enough to excite electrons to vibronic states that cause the material to emit a fluorescence signal<sup>20</sup>. Thus working with longer wavelength lasers, usually in the near-IR region, reduces fluorescence. Unfortunately, near-IR lasers don't completely eliminate fluorescence in materials that strongly absorb light in near-IR, such as polycyclic aromatic compounds and transition metal complexes<sup>8</sup>. Moreover, other problems related to sensitivity and self-absorption are associated with using near-IR lasers: the intensity of scattered Raman signal is inversely proportional to 4<sup>th</sup> power of excitation laser wavelength which means that using longer wavelength such as Nd:YAG laser at 1064nm leads to dramatic drop in the scattered light intensity and consequently require more sensitive detectors and higher power lasers; also, the shifted Raman signal also falls in the near-IR region and could be absorbed by the sample itself which could attenuate the Raman intensity<sup>20</sup>.

The fluorescence signal is much stronger than Raman signal that could be easily masked; and so, it is important to reduce the fluorescence to the minimum possible limit. The following approaches could be used to compact fluorescence:

- 1) If the sample includes impurities that emit fluorescent light, then the impurities should be removed if possible or bleached out by irradiating them by strong laser for long time<sup>8</sup> which is not applicable in this project.
- 2) In case of fluorescent sample, using laser source with wavelength in the near-IR region could solve the problem.
- 3) Due to high quantum efficiency and sensitivity of the CCD detectors even in the near-IR region up to 1000nm<sup>7,8</sup>, near-IR laser coupled with CCD detector could be employed to measure fluorescent samples<sup>23</sup>.
- 4) Pulsed laser could be used to discriminate the fluorescence signal from the Raman signal since the life time of Raman is order of magnitude shorter than the fluorescence; by employing an electronic gate on the detection system it would be possible to isolate the Raman signal and measure it<sup>8</sup>; however, using this technique is outside the budget for this project.

Based on the above discussion, the 785nm diode laser with 500mW from RGBLase LLC has been selected; the following points summarize why this laser source has been chosen:

- 1) The 785nm wavelength falls in the near-IR region, which is very important to reduce the fluorescence from the opaque petroleum pitches.
- 2) The drop in Raman intensity associated with this wavelength due to the 4<sup>th</sup> power frequency dependence have been compensated by using highly powered laser source of 500mW.
- 3) This wavelength is within the high quantum efficiency range for the CCD detector.
- 4) The self absorption of Raman signal by the sample itself could be a major problem when using near-IR region; the following points should be considered in order to minimize the self absorption effect associated with near-IR excitation: (a) a stronger shorter near-IR wavelength should be selected i.e. 785nm laser not 1064nm laser (b) the laser should be focused on the sample-sapphire window interface and should be close the reactor wall to minimize the sample depth

(sample thickness) parameter that shows up in Lambert-Beer law that governs the absorption spectroscopy<sup>8</sup>.

- 5) This laser module provides fiber coupling option, very low optical noise, stabilize laser wavelength and very narrow spectrum width of less than 0.2nm in a highly integrated laser unit with laser optics and electronics enclosed in small single package.

Figure (4.9) shows a top view of the fiber-coupled 785nm Raman Laser Module used in this system.



Figure 4.9: Top view of the fiber coupled 785nm Raman Laser Module from RGBLase LLC.



### 4.3.3 Spectrometer

The spectrometer includes two main components: the spectral analyzer and the detection system. The function of the spectral analyzer is to separate the multi-chromatic scattered light into its individual monochromatic light that then detected and quantified by the detector. There are two types of spectrometers: the dispersive spectrometer that is based on diffraction grating technology, and the interferometric spectrometer that is only used with FT-Raman spectroscopy; the attention will be focused toward the dispersive spectrometer since it is the one that is used in this system.

#### 4.3.3.1 Monochromator Vs. Spectrograph

The dispersive spectrometer could be either monochromator-based or spectrograph-based instrument<sup>7</sup>. Monochromator-based instruments selectively transmit a specific Raman wavelength and reject all the other wavelengths while the spectrograph-based instruments direct all of the wavelengths to multichannel detector<sup>7</sup>.

Typically, the monochromator-based spectrometers consist of an entrance slit, collimated mirror, diffraction grating, focusing mirror and exit slit. The diffraction grating is the heart of the monochromator since it is where the light gets separated; the diffraction grating is an optical element made of many equally spaced grooves<sup>8,20</sup> on a transmissive or reflective plane<sup>7</sup>; these grooves are spaced a distance equal to the wavelength of the light to be analyzed<sup>20</sup>. When the polychromatic light hits the grating, light diffraction occurs and the light leaves the grooves as secondary waves that could either constructively or destructively interfere; this interference produces spatially separated monochromatic wavelengths. In order to focus a specific wavelength at the exit slit, the path difference in which that specific wavelength is diffracted should be equal to the wavelength ( $\lambda$ ) of that selected light or its integer<sup>20</sup>. The other wavelengths destructively interfere and are not focused at the exit slit. The path difference depends on the distance between the grooves, the angle of incidence ( $\alpha$ ) and the angle of reflection ( $\beta$ )<sup>20</sup> in the case of reflective grating; figure (4.10) depicts this concept. To focus other wavelengths at the exit slit, a scanning mechanism rotates the diffraction grating causing constructive

interference for other wavelengths and the scanning proceeds until the desired spectrum is covered.

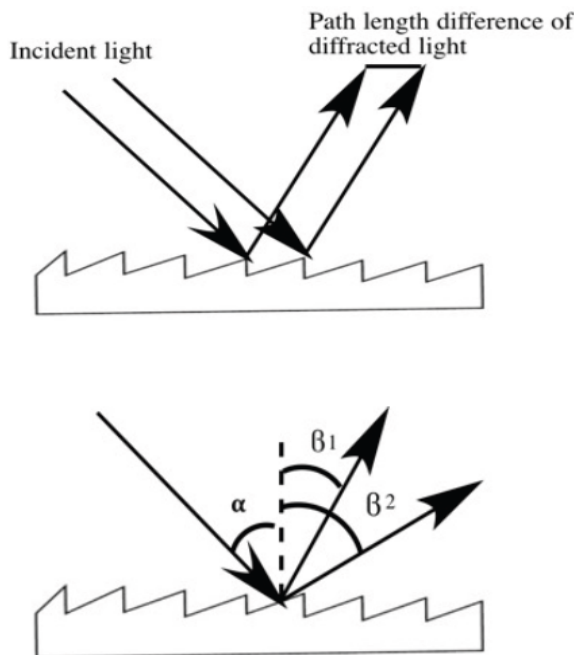


Figure 4.10: schematic of diffraction grating.

It is obvious that this scanning process is time consuming and is not suitable for short-lived unstable molecules<sup>8</sup>; this was the motivation behind developing the spectrograph with a multichannel detector. On the other hand, the single monochromator suffers from poor stray light rejection which could overwhelm the weak Raman signal<sup>8</sup>; the stray light is formed by the scattered excitation wavelength (Rayleigh signal) and the undiffracted scattered light<sup>6,8</sup>. Thus, double monochromators and triple monochromators have been introduced in order to significantly improve the stray light rejection<sup>6,8</sup>; the double monochromator has done a superior job in reducing stray light by introducing an intermediate slit between the two monochromators<sup>6</sup>; the signal emerges from the first monochromator is filtered by the second monochromator<sup>8</sup>; this improvement in stray light has enabled observation of Raman bands very close to excitation laser line<sup>6,8</sup>. The triple monochromators is much superior than double monochromators in eliminating the stray light but the triple monochromators has much lower optical throughput and most of

the Raman signal is lost<sup>7</sup>. The scanning multistage monochromators coupled with photomultiplier tube detector, which will be mentioned later, was the standard dispersive Raman instrument before the introduction of spectrograph with array detector<sup>6</sup>; figure (4.11) is depicting a schematic of double monochromators.

As mentioned earlier, the spectrograph-based spectrometer is the other dispersive type spectrometer. Basically, the spectrograph is a single monochromator coupled with multichannel array detector; the filtration of the stray light is achieved in this case by utilizing a stray light filter not by coupling multiple monochromators. In most cases, the filter is a holographic notch filter or a dielectric band filter<sup>20</sup>. The notch filter is the best in stray light filtering<sup>8</sup>. Notch filters are constructed by simultaneous recording of interference pattern between two sinusoidal wave mutual lasers onto multiple film layers<sup>8</sup>; this filter features high optical density, very narrow spectral width and is free from extraneous reflection bands<sup>8</sup>. The spectrograph dramatically improves the signal to noise ratio (S/N) by taking advantage of multichannel detection, and by offering better optical throughput because of single grating<sup>20</sup>; the dispersed light coming from the grating is focused on a two dimension photo-sensing array that consists of hundreds of pixels where each pixel detects different spectral band<sup>20</sup>. The most popular spectrograph is the Czerny-Turner spectrograph; a schematic of this spectrograph is shown in figure (4.12).

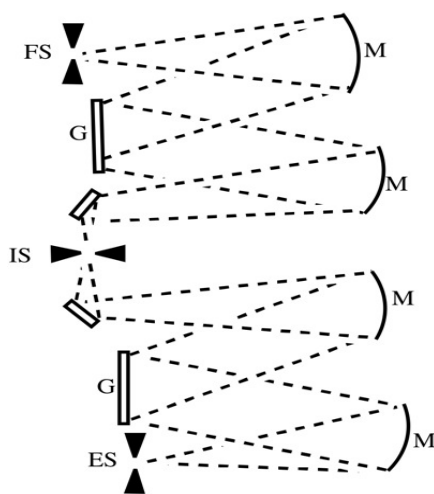


Figure 4.11: schematic of double monochromator. ES: entrance slit; IS: intermediate slit; ES: exit slit; M: mirror; G: diffraction gratings.

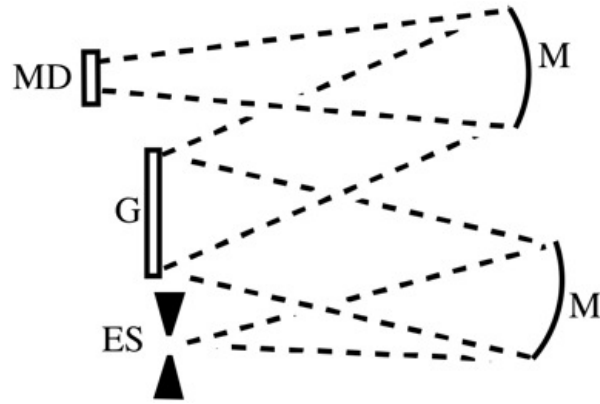


Figure 4.12: schematic of Czerny-Turner spectrograph; ES: entrance slit; M: mirror; G: diffraction grating; MD: multichannel detector.

#### 4.3.3.2 Spectrometer Efficiency

The spectrometer efficiency is determined by the two conflicting parameters: the optical throughput and the spectral resolution; the optical throughput power and the spectral resolution are related by the F-number equation<sup>7,8</sup> :

$$F = f/D \quad \text{Equation (4.1)}$$

$f$  is the focal length of the collimated mirror and  $D$  is calculated from the side length of the grating,  $L$ , by equation (4.2):

$$D = 2L/\sqrt{\pi} \quad \text{Equation (4.2)}$$

The smaller the F-number, the higher the optical throughput; this could be achieved by decreasing the focal length and widening the grating. The smaller the focal length  $f$ , however, the lower the resolution. To maintain higher resolution with small  $f$ , a wider more expensive slit is required; typical F numbers for grating are between 5 and 10<sup>8</sup>. Furthermore, the groove density is another factor that determines the resolution; the higher the groove density, the higher the resolution but the lower the spectral coverage<sup>8</sup>. In order to cover a wider spectral range while keeping a higher resolution for array detectors, the Raman beam can be divided by beam splitters into sections and each section is separately detected. All of the sections are stacked together to give the whole spectral range<sup>7</sup>.

### 4.3.3.3 Detectors

Three dominant types of detectors have been used by the Raman spectroscopic community: the interferometer, the photomultiplier tube (PMT) and the charge-coupled device (CCD)<sup>6,8,20</sup>; the interferometer is limited to FT-Raman instrument and will not be discussed here; on the other hand, the PMT was the standard detector for dispersive system until the 1980s and it will briefly mentioned here; the CCD is the most advanced detection system for dispersive detectors currently being used and it will be described in detail.

The PMT is a single detector which means it can only detect one spectral band and can't detect simultaneous bands; the PMT coupled with scanning monochromators was the standard spectrometer before the introduction of multichannel detector<sup>6</sup>. The PMT is a photon-sensing instrument that converts a photon beam to electrical current: when the photon strikes the photo-sensitive material (photocathode) in the tube, the energy of the photon will release electrons from the photocathode and these electrons release more electrons from the following dynodes; the resulting electrical signal is collected by the anode as an output signal<sup>8</sup>. The sensitivity of the PMT is wavelength dependent<sup>8</sup> with shorter the wavelength, the better the sensitivity. Poor sensitivity is one reason why PMT wasn't used with long wavelengths, namely near-IR wavelengths. Instead of PMT, CCDs and interferometers are used for Raman spectroscopy.

Currently, the CCDs are the most advanced and popular detectors used for Raman spectroscopy<sup>7</sup>. The CCD is a two dimensional array detector made of silicon based photo-sensitive devices<sup>6-8</sup>. Each device or pixel in a CCD produces electrons upon interaction with a photon and these electrons are stored (charged) in its pixel until a readout mechanism converts them to a digital signal that is processed by a computer<sup>6-8</sup>. A sketch of a CCD detector is shown in figure (4.13). The CCD detector offers attractive features that are summarized by the following points:

- 1) It is usually coupled with notch filter to eliminate the stray light and with a single monochromator; this allows for smaller compact designs and higher optical throughput.
- 2) The detector offers fast simultaneous detection of all Raman wavelengths instead of the long scanning mechanism.

- 3) The quantum efficiency and the sensitivity for the CCD detector is high in the range 120-1000 nm<sup>7,8</sup>; therefore, the CCD detector coupled with near-IR laser, such as the case in this project, could be used with fluorescent compounds<sup>8</sup>. Although, the quantum efficiency of the detector drops as the wave lengths of scattered light approach the band-gap of silicon, at 1100nm<sup>6-8</sup>, the efficiency is still approximately 20% efficiency at 1050nm<sup>7</sup>.
- 4) The sensitivity of the CCD detector could be further improved by modifications of the device structure such as thinning of the device and back-illumination<sup>6</sup>.
- 5) The CCD detector is free from noise except a little read out noise<sup>8</sup>; the readout noise is the noise associated with reading the digital signal.

All these attractive features significantly improve the S/N ratio and revolutionized the Raman measurements.

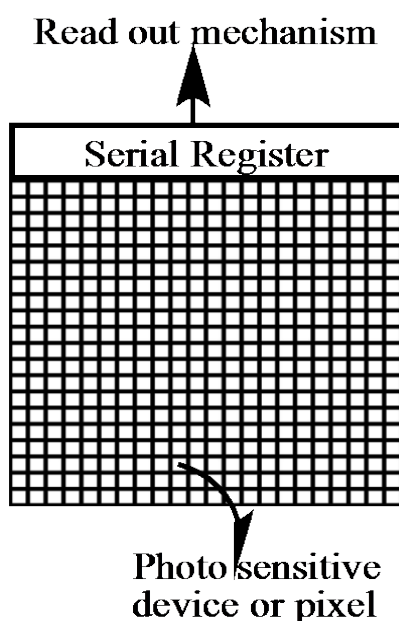


Figure 4.13: schematic of CCD detector

#### 4.3.3.4: The Selected Spectrometer

Due to the attractive features for spectrographs and CCD detectors, a scientific grade Raman spectrometer, model QE65 Pro-Raman, from Ocean Optics was selected; this spectrometer has the following characteristics:

- 1) Symmetrical crossed Czerny-Turner spectrograph with 101.6m focal length (input and output) that provides compact design.
- 2) Two-dimensional back-thinned CCD detector from Hamamatsu, model S7031-1006, with 1064×64 pixels; the detector is preconfigured for 785nm excitation laser.
- 3) Model H36 diffraction grating with 900 mm<sup>-1</sup> groove density that covers a 0 cm<sup>-1</sup>-2040 cm<sup>-1</sup> (785 nm-934 nm) spectral range and provides 6 cm<sup>-1</sup> of resolution; a wider spectral range up to 3950 cm<sup>-1</sup> could be obtained by using lower groove density diffraction grating.
- 4) Thermally stable detector with low noise and low dark signal; the detector is cooled down to -15°C which enables low light detection applications and long integration time from 8 milliseconds to 15 minutes.
- 5) The detector provides high quantum efficiency from 40% to 80% in the configured spectral range; this offers improved S/N ratio of more than 1000:1; figure (4.14) shows the quantum efficiency curve for this detector.
- 6) The spectrometer is fiber optics coupled and coming with replaceable entrance slits that offers further flexibility in adjusting the optical throughput and the resolution.

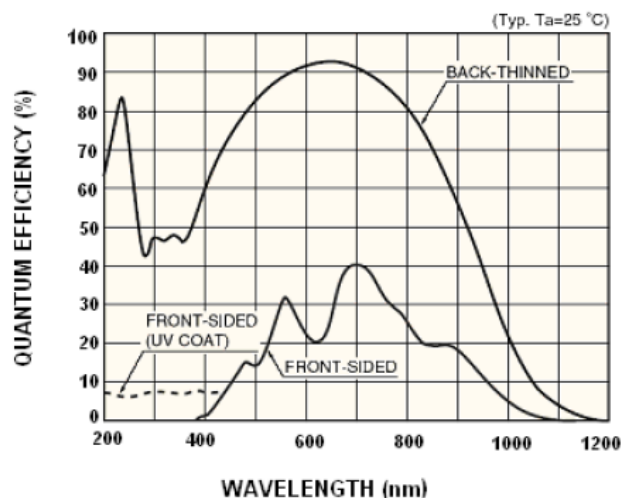


Figure 4.14: quantum efficiency curve for back-thinned CCDs detector from Hamamatsu, model S7031-1006 (adopted from Ocean Optics, Inc.)

#### **4.3.4 Sample Illumination And Collection System**

The sample illumination and collection system delivers the excitation laser and focuses it on the sample and then collects the backscattered light and sends it to the detector. Importantly, the excitation laser light should be conditioned prior to be sent to the sample and the backscattered light should be filtered from the excited laser line (the Rayleigh scattering) before being detected<sup>7</sup>. Conditioning of the incident laser involves filtering the laser from any unwanted frequencies such as plasma lines and any fluorescence generated from the laser gain medium or from the fiber optics<sup>7</sup> and adjusting the polarization. The collected light must be filtered from the excited laser line. There are two collection geometries used to collect the backscattered Raman light: the parallel configuration where the backscattered light and the excited laser are aligned 180° from each other, and the perpendicular configuration where the backscattered light and the excited laser are aligned 90° from each other<sup>7,8,20</sup>.

The sample illumination and collection systems that have been implemented in this work consist of the following items:

- a- Polarization probe with separate parallel and perpendicular light channels.
- b- Excitation and collection fiber optics.
- c- Three-dimensional motorized stage.

##### **A. The Polarization Probe**

The polarization probe enables polarized Raman data to be obtained that yields information on the molecular orientation and the molecular structure of the molecules under investigation. A fiber coupled polarization probe from InPhotonics Inc. has been used in this project. The probe includes polarizing filter for the excited light and wavelengths filters for the collected light. The polarization probe presented in figure (4.15) consist of the following elements:

- 1) Excitation channel: this channel includes a plain polarizer (filter) that allows only the light polarized in the plain of incidence to pass (p-polarized or parallel component) and reject the light polarized perpendicular to the plain of incidence (s-polarized or perpendicular component); the plain of incidence refers to the



- plain that is spanned between the direction of light propagation and the vector normal to polarizer surface. Moreover, this channel includes a wavelength filter to remove any spectral contribution from the quartz of the fiber optic.
- 2) Sampling lens: this lens is dual function: it focuses the polarized light on the sample and then collects the backscattered light from the sample; it is replaceable lens with different focal lengths specifically 10mm and 20mm.
  - 3) Rayleigh filter: this filter removes the backscattered light that have the same frequency as the excitation laser; the optical density of this filter is greater than 6. This means that it can remove more than 6 orders of magnitude of the incoming intensity.
  - 4) P-polarized collection channel: this channel includes a filter that passes only the parallel component of the backscattered light.
  - 5) S-polarized collection channel: this channel includes a filter that passes only the perpendicular component of the backscattered light.

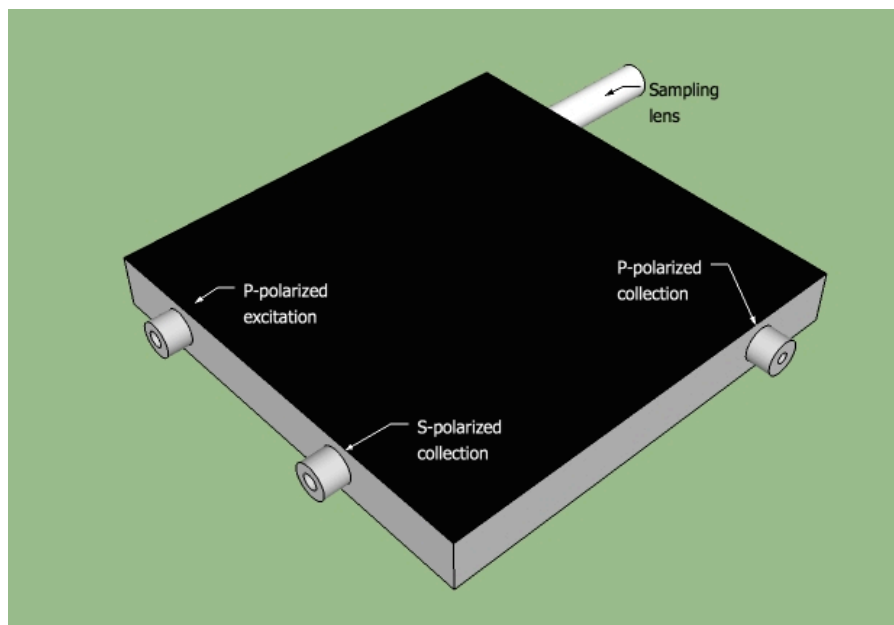


Figure 4.15: Sketch of the polarization probe

## **B. Excitation And Collection Fiber Optics**

The fiber optics technology have revolutionized the Raman measurements specifically for on-line monitoring of remote chemical processes that are conducted in severe environments<sup>7,8</sup>; these measurements have become possible because the fiber optics can transmit the light very efficiently to far distance without loss of information. The fiber optics are ideal optical tubes that transfer optical signal to the sample and from the sample<sup>8</sup>; the fiber optic is constructed from two materials with different refractive indices<sup>8</sup>; the higher refractive index material forms the inner core while the lower refractive index material forms the outer cladding. The optical signal is preserved by total reflection at the core-cladding interface<sup>8</sup>.

In this work, the excitation laser has been delivered to the sample via a 100  $\mu\text{m}$  fiber optic while the backscattered light have been sent to the detector via a 500  $\mu\text{m}$  fiber optic since it is important to have wider cross section for the collecting fiber<sup>7</sup>.

## **C. Three-Dimensional Motorized Stage**

In order to precisely and easily align the polarization probe with the reactor, a three-dimensional motorized stage, model MTS50-Z8, from Thorlabs Inc. has been used; this stage provides an accurate, smooth, and computer controlled motion in three Cartesian axes (x, y and z); the stage can move 50mm in the three axes simultaneously with 0.29 nm resolution and 0.1  $\mu\text{m}$  minimum movement; also, it can carry 4.5 Kg of load in the vertical direction (z) and 12 Kg in horizontal directions (x and y). The polarization probe has been attached to the vertical stage (z-stage) whereas this stage controls the penetration depth of the laser light through the reactor while the other two stages, x and y stages, control the transverse position (horizontal) of the laser on the reactor; the stage has been fixed to the optical table via mounting adapter. Figure (4.16) shows the polarization probe mounted on the motorized stage.

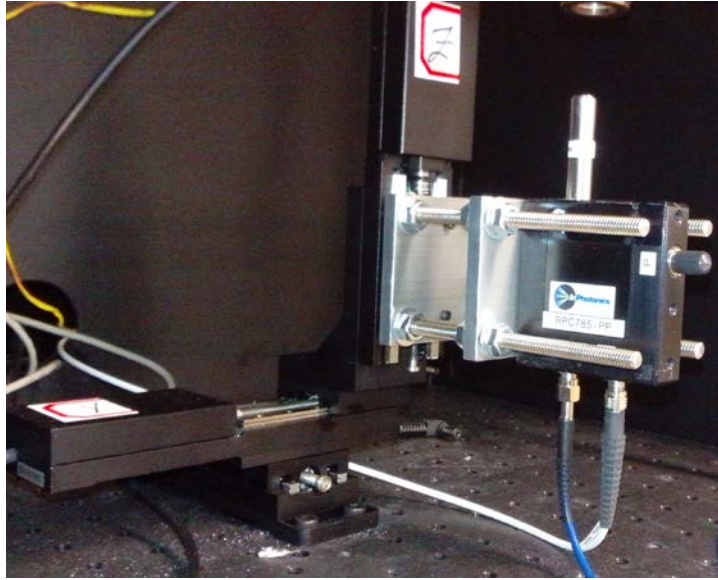


Figure 4.16: the polarization probe mounted on the motorized stage

## Chapter 5: Materials And Methodology

### 5.1 Materials and Chemicals

In the course of implementing and validating the current system, several chemicals have been used as reactants, solvents, catalyst, and gas chromatography gases.

Benzothiophene from Aldrich Canada, 99% purity, has been used as a sulfur model compound for the *in-situ* and *ex-situ* HDS reactions.

Ni-Mo/ $\gamma$ -Al<sub>2</sub>O<sub>3</sub> catalyst, denoted as DN-200 from Criterion Catalysts with an average diameter of 1.5, mm has been utilized for HDS reactions. This catalyst composes of 67-77 wt.% of aluminum oxide, 10-14 wt.% nickel oxide, 12-19 wt.% of molybdenum oxide, and 1-4 wt.% phosphorus pentoxide<sup>13</sup>. The catalyst had being pre-sulfided at 193°C for 24 hour and then at 343°C for 24 hour using atmospheric gas oil that contains 2.9 vol% of butanethiol. Following sulfidation, the catalyst had being pre-coked (stabilized) with heavy gas oil feed for 7 days at a temperature of 375°C, a pressure of 8.8 MPa, and LHSV of 1 h<sup>-1</sup>; after pre-coking, the catalyst was transported and kept in a glove box under inert atmosphere for later use. The pre-coked pre-sulfided catalyst had been provided by Synrcude Canada.

As a solvent for HDS reaction, 1-Methylnaphthalene from Acros Organics of 97% purity, has been used as received. On the other hand, Toluene of 99.5% purity from Acros Organics and dodecane of 99.5% purity from Acros Organics have been utilized as solvents for establishing a calibration curve to be used in quantitative analysis. These solvents have been used as received.

In terms of gases; research grade hydrogen from Praxair Canada Inc., extra dry air from Praxair Canada Inc., and ultra high purity helium from Praxair Canada Inc. have been employed for gas chromatography analysis. On the other hand, research grade hydrogen from Praxair Canada Inc. has been employed for hydrotreating, while research grade nitrogen from Praxair Canada Inc. has been utilized for reactor purging

## **5.2 Methodology**

The In-situ Raman hot stage reactor (viewport micro-reactor) that has been developed in this work is designed for on-line monitoring of mesosphere formation phenomena and the chemical reactions associated with it. Before studying the mesosphere formation with this reactor, the viewport micro-reactor itself must be verified and validated by comparing its results with other reliable techniques. The validation process is necessary to trust the outcome of this system and to finally have a dependable instrument.

Firstly, the system has been verified to collect the Raman signal for non-reactive chemicals by measuring the spectra of some solvents and comparing the collected data with the literature. Secondly, the system has been used to establish a spectral calibration curve for quantitative analysis: the Raman signals have been collected for different concentrations of toluene in dodecane binary mixture; these spectra have been analyzed later to build the calibration curve. After that, the viewport micro-reactor has been verified to investigate a model reaction namely the HDS of benzothiophene. This reaction has been conducted at ex-situ and in-situ conditions. The ex-situ reaction has been done in a micro-batch reactor and the products of this reaction have been analyzed using GC/MS. On the other hand, the in-situ reaction was being done in the viewport micro-reactor while the Raman spectra were being collected; also, the products of the in-situ reaction have been analyzed by GC/MS technique. The results of the ex-situ and in-situ reactions have been compared to verify the reliability of the viewport micro-reactor.

## **5.3 Experimental Procedures**

### **5.3.1 Preliminary Acquisition Procedures**

Prior to collect the Raman data, the system should be prepared to ensure that the optimum Raman signal is obtained. The preparation involves: laser-sample alignment, selection of optimum data acquisition parameters, and subtraction of dark spectrum.

### **5.3.1.1 Laser-Sample Alignment**

The initial laser alignment is done while the laser is switched off and the light enclosure is opened. The x and y stages of the probe are manually controlled to align the probe tip with the center of the viewport micro-reactor; next, the tip of the probe is covered with small piece of thin paperboard to protect the tip during the alignment; the z stage is moved up until the probe's tip almost touches the sapphire window; this is almost the zero position. The z stage is then moved down 10 mm or 20 mm as required and the paperboard is removed. After this initial alignment, the light enclosure is closed and the laser is switched on and this is important to ensure that the operator is safe while the laser is operating. Afterwards, the transverse position of the laser is scanned until the strongest spectrum is obtained; the optimum transverse position is usually very close to the edge of the viewport micro-reactor. Next, the z stage is then slightly moved down and up until the optimum position is obtained; the optimum position is reached by looking at the Raman spectrum graph and note the coordinate that gives the maximum intensity. The optimum x-y-z coordinate is recorded for further use.

### **5.3.1.2 Optimum Acquisition Parameters**

Three acquisition parameters should be selected prior to acquisition of Raman spectra. These parameters are: the integration time, the scan to average, and the boxcar width. The integration time refers to the time over which the spectral intensity is integrated by the detector. The longer the integration time, the higher the intensity and vice versa. The criteria to setup the integration time is to increase it until the strongest band on the Raman spectra graph reaches approximately 75% of the detector limit. On the other hand, the scan to average refers to the number of discrete spectral acquisitions that are accumulated prior to be averaged to a single acquisition; the higher the scan to average, the better the S/N ration. Finally, the boxcar width determines the smoothness of the spectra; the boxcar width averages the spectra of the adjacent element on the detector. The higher the boxcar width the smoother the spectra and the better S/N ratio but the lower the resolution.

### **5.3.1.3 Subtraction of Dark Spectrum**

After setting the optimum position of the laser and the acquisition parameters, the dark spectrum is ready to be subtracted. The dark spectrum is the spectrum taken while the laser path is blocked. This spectrum could be thought as the spectral response (contribution) of the optical elements present in the Raman system. This spectrum should be subtracted. While the laser is switched on, the laser is moved away from the viewport micro-reactor by shifting the x or y stage and keeping the z stage stationary; the laser should be moved until the laser is shined to free space inside the closed dark enclosure; the dark spectrum is then saved and subtracted. The other way to save the dark spectrum is to block the laser light path and then save and subtract the dark spectrum. Both ways have given the same result. After subtracting the dark spectrum, the optimum position of the laser is then restored and the system becomes ready to measure the Raman signal.

### **5.3.2 Validating Raman Spectra For Non-Reactive Systems**

In order to verify the reliability of this system to produce correct Raman signals, the system has been used to generate Raman signal for toluene. The collected spectrum has been compared with published spectrum in the literature.

1 ml of toluene has been placed inside the viewport micro-reactor, which has then been sealed without inserting the magnet; next, the viewport micro-reactor has been firmed vertically and longitudinally above the polarization probe using a clamp. Afterward, the preliminary acquisition procedures mentioned earlier have been applied to obtain the Raman signal for toluene.

It is important to mention that before measuring spectra, the spectral contribution from the empty viewport micro-reactor, specifically from the sapphire window, has been investigated. The Raman signal has been obtained for the sapphire window by the shining the laser into it while the reactor was empty.

### 5.3.3 Establishing Spectral Calibration Curve For Quantitative Analysis

Firstly, preliminary acquisitions procedures, which have been mentioned in section (5.3.1), have been applied to prepare the system for acquiring Raman spectra; next, the Raman spectra for dodecane and toluene have been acquired separately. Afterwards, both spectra have been overlaid at the same graph in order to find the strongest unique band that is in toluene and is not in dodecane; this band is located at  $628\text{ cm}^{-1}$  in this case. Diluted solutions of different concentration of toluene in dodecane have been prepared and the Raman spectra for them have been acquired. The mixtures concentrations are 12.26 wt., 2.04 wt.%, 1.12 wt.%, 1.10 wt.%, 0.81 wt.% and 0.61 wt.%. The  $628\text{ cm}^{-1}$  band has been observed to track the existence of toluene in the binary mixture of toluene in dodecane. This unique band has been disappeared at concentration lower than 0.61wt%. The calibration curve that relates the intensities of this unique band and the concentrations of toluene has been established.

### 5.3.4 Ex-Situ HDS Reaction Of BT

A solution of 5 grams of 2 wt.% of BT in 1-methylnaphthalene have been loaded in 15 ml micro-batch reactor shown in figure (5.1). This reactor is made of Swagelok stainless steel tube of 12.7 mm diameter and 0.711 mm thickness. Afterward, the micro-batch reactor has been loaded with 0.2 gram of 125mesh DN-200 catalyst (4wt.% of catalyst in the feed). The reactor has been sealed, purged with nitrogen at 5 MPa and then preliminary tested against leak using snoop liquid; next, hydrogen at 5 MPa has been used to purge and pressurize the reactor which has been then tested against leak using snoop liquid and hydrogen detector. After that, the pressure has been then lowered to 2.5 MPa and the reactor has been disconnected from hydrogen cylinder and emerged into the hot sand reciprocal saw shaker that has been adjusted at  $290^{\circ}\text{C}$ . The hot sand reciprocal saw shaker is shown in figure (5.2). The reaction has been proceed for 20 min; after that, the reactor has been taken out from the sand bath and cooled for 1 min using compressed air and then quenched in water. The reactor has been then depressurized from gases inside the fume hood. Finally, the reaction products have been filtered out using  $0.45\text{ }\mu\text{m}$  filter and then saved for analysis. The same reaction has been repeated several times but



for longer periods in order to track the conversion of the BT and the intermediates. The reaction has been repeated for 40 min, 60 min, 80 min, 100 min, 120 min, 4 hours and 6 hours.



Figure 5.1: The micro-batch reactor that has been used for ex-situ reactions.



Figure 5.2: The micro-batch reactor emerged into hot sand reciprocal saw shaker.

### **5.3.5 In-situ HDS Reaction of BT**

Firstly, the nut that fixes the sapphire window in the viewport micro-reactor has been disassembled and the reactor's valve has been closed. Afterward, 1 gram of 2 wt.% of BT in 1-methylnaphthalene and 0.04 grams of pelleted DN-200 catalyst has been loaded in the viewport micro-reactor (4 wt.% of catalyst in the feed). This reaction feed is the same

as the reaction feed of the ex-situ runs. The magnet has been then inserted into the thermocouple tip; 1mm height stainless steel washer has been placed over the magnet. This washer creates a space between the magnet and the sapphire window otherwise the magnet would touch the sapphire and significantly weaken the Raman signal from the reaction mixture. The reactor has been then reassembled in the sequence shown in figure (4.7). After that, the reactor has been sealed, purged with nitrogen at 5 MPa and then preliminary tested against leak using snoop liquid; next, hydrogen at 5 MPa has been used to purge and pressurize the reactor which has been then tested against leak using snoop liquid and hydrogen detector. The pressure has been then lowered to 2.5 MPa and the reactor has been disconnected from hydrogen cylinder. Subsequently, the reactor has been wrapped with several layers of steel foam followed by the heating tape, as shown in figure (4.8), and finally with a thick layer of insulation material as shown in figure (5.3). Later on, the reactor has been firmed vertically and longitudinally above the polarization probe using a clamp as shown in figure (5.4). The thermocouple has been connected to the external temperature controller and the external magnet has been turned on. Subsequently, the aforementioned preliminary acquisition procedures in section (5.3.1) have been followed to prepare the system for acquiring Raman spectra. Once the temperature controller has been switched on to heat up the reactor, the time domain Raman spectra for the reactive mixture have been acquired via the p-polarized collection channel. The Raman spectra have been acquired over three phases: the heating phase is for Raman spectra collected over the heating period which is the period to get from room temperature up to the reaction temperature, the reaction phase is for Raman spectra collected during the reaction time which is 4 hours, and the cooling phase is for Raman spectra acquired over the cooling period which is the period to get from the reaction temperature down to the room temperature. The reaction products have been saved for analysis.

In order to study the molecular orientation and the depolarization ratio, this reaction has been repeated under the same conditions except the Raman spectra have been collected via s-polarized channel this time.



Figure 5.3: Wrapping the insulation material over the heating tape.

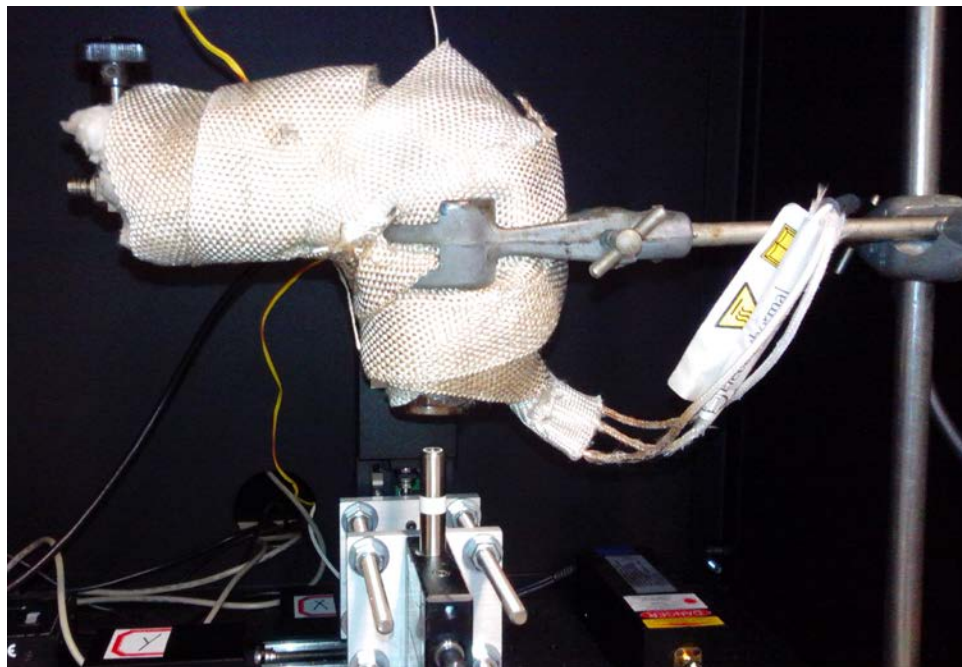


Figure 5.4: The hot stage reactor mounted over the polarization probe.

### 5.3.6 Products Analysis

The products of HDS reactions of BT have been analyzed and identified using GC/MS technique. The Agilent 7890A gas chromatograph has been used to quantify the reaction products and to separate them based on their retention time. This gas chromatograph is of 250  $\mu\text{m}$  column diameter and of 0.25  $\mu\text{m}$  coating thickness. The following experimental conditions have been used in the GC analysis: the carrier gas is helium with 2 ml/min volumetric flow rate; the split ratio is 100:1; the injection temperature is 250°C while the injection volume is 0.2  $\mu\text{l}$ ; the oven starts at 75°C for 0.5 min and the final temperature is 280°C with 10°C/min ramp; the detector is FID type adjusted at 300°C with hydrogen flow of 35 ml/min, 400 ml/min air flow and 28 ml/min make up flow from the helium. On the other hand, MS technique has been used to identify the reaction products based on their molecular mass; and so, one sample of reaction products that includes the maximum number of components have been sent for MS analysis to the Analytical and Instrumentation Lab located in the Gunning/Lemieux Chemistry Centre at University of Alberta.

## Chapter 6: Results and Discussion

### 6.1 Preprocessing of Spectral Data

The analytical signal during in-situ Raman spectroscopy consist of chemical information, background and random noise<sup>24</sup>. Therefore a preprocessing algorithm is needed to remove the background and to distinguish between the signal (chemical information) and the noise. In order to extract valuable information from Raman spectra, the underlying fluorescence background that could easily distort the Raman spectra should be removed prior to any further analysis. Different preprocessing methods have routinely been used to eliminate the baseline drift in spectroscopic signals<sup>24</sup> including:

- Polynomial fitting
- Penalized least square
- Wavelet transforms
- Robust local regression

Two baseline correction algorithms have been proposed to deal with the spectra obtained in this work, continuous wavelet transforms with a penalized least squares approach (CWT) and adaptive iteratively reweighted Penalized Least Squares (airPLS). The first candidate is the algorithm based on continuous wavelet transforms and penalized least square approach<sup>25</sup>; this algorithm is called in short by CWT algorithm. The penalized least square approach is a smoothing and fitting method that balances between data fidelity and fitting roughness to establish data fit<sup>24</sup>. The tradeoff in this approach is that the smoother the fit, the less precise and vice versa. A smoothing parameter ( $\lambda$ ) is used to tune the smoothness vs. the fidelity of the fit; the larger is  $\lambda$ , the smoother the fit but the less accurate. In general, a major challenge in fitting a baseline is to fit the data in the non-peak sections and to leave the peak segments without fitting. With the CWT algorithm, this issue has been solved by transforming the data into wavelet space where the peaks are detected and then their width are estimated by continuous wavelet derivative calculation<sup>24,25</sup>. Based on simulated and experimental results, the CWT algorithm provides an accurate, valid and tunable preprocessing tool to efficiently correct the baseline for highly fluorescent spectra; this algorithm can also deal with negative

peaks that originate from peak shoulders and overlapping peaks by special treatment<sup>24,25</sup>. This algorithm is slow especially for two-dimensional datasets<sup>24</sup>. Due to the slow data processing times, this algorithm was excluded due to the large number (thousands) of spectra that were generated during this project. The other method evaluated in this work was the airPLS algorithm which utilizes iterative procedures to estimate the weight vector of fidelity, introduced by Zhang<sup>25</sup> and Cobas<sup>26</sup>, to assign peak and non-peak segments but without transforming the data into the wavelet domain<sup>24</sup>; the weight of iterations are governed by the square of sum errors (SSE) between a previously fitted baseline and the original data while the smoothness of the fit is controlled by a penalized least square principle that is similar to the one described in the CWT method<sup>24</sup>. Depending on simulated and experimental results, the airPLS algorithm can be an extremely fast, accurate, flexible and reliable baseline correction algorithm that can successfully correct the baseline for large dataset of high fluorescent spectra. Importantly this algorithm is sensitive in low signal to noise environments since the algorithm shows better baseline correction for small peaks over other algorithms<sup>24</sup>. Because of its superior speed over CWT algorithm, its minimum tunable parameters, and much simpler mathematical background; the airPLS algorithm is used throughout this study as baseline correction algorithm; figure (6.1) shows a background removed by CWT and airPLS algorithms.

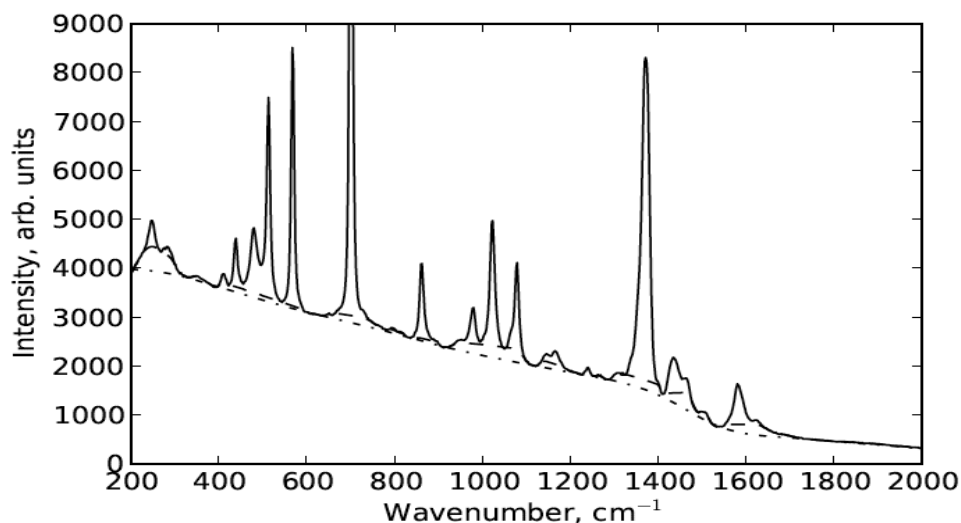


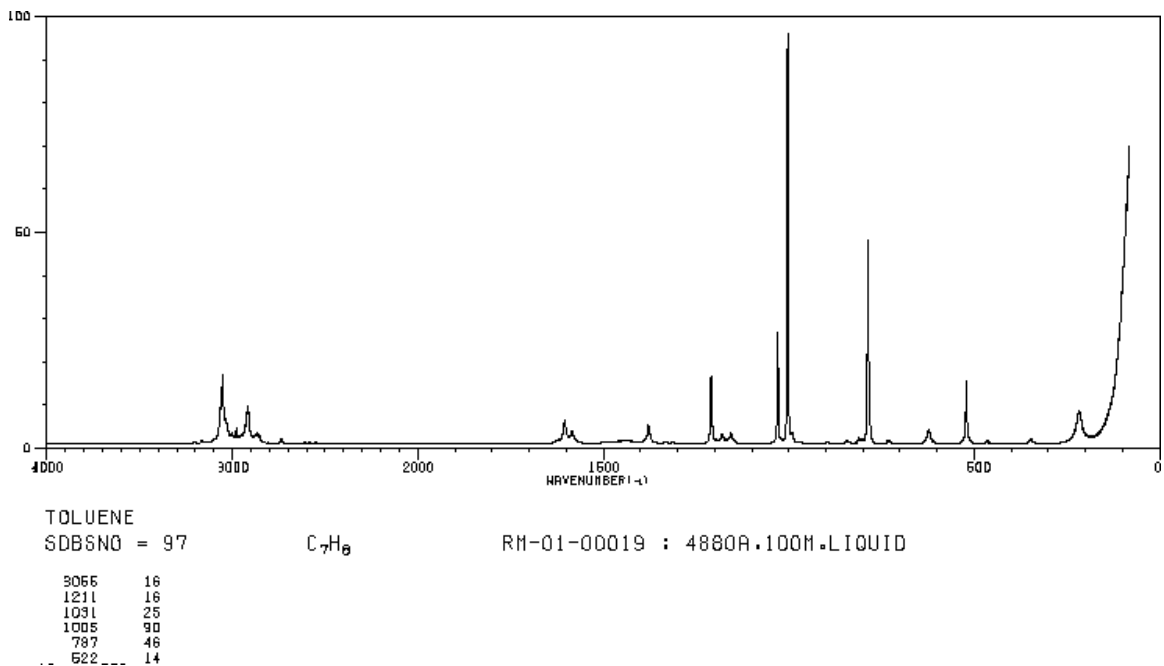
**Figure 6.1: Original and baseline corrected spectrum using CWT and airPLS algorithms; the continuous curve is the raw spectrum without preprocessing; the dash dotted fit is the baseline fitted using airPLS algorithm with the following parameters:  $\lambda = 10^5$  and order of square difference = 2; the dashed line is the fitted background using CWT algorithm with the following parameters: threshold = 0.5,  $\lambda = 100$ , SNR = 1 and ridge length = 5 (figure courtesy of Michal Nipcon).**

## 6.2 Validating The Collected Raman Spectra

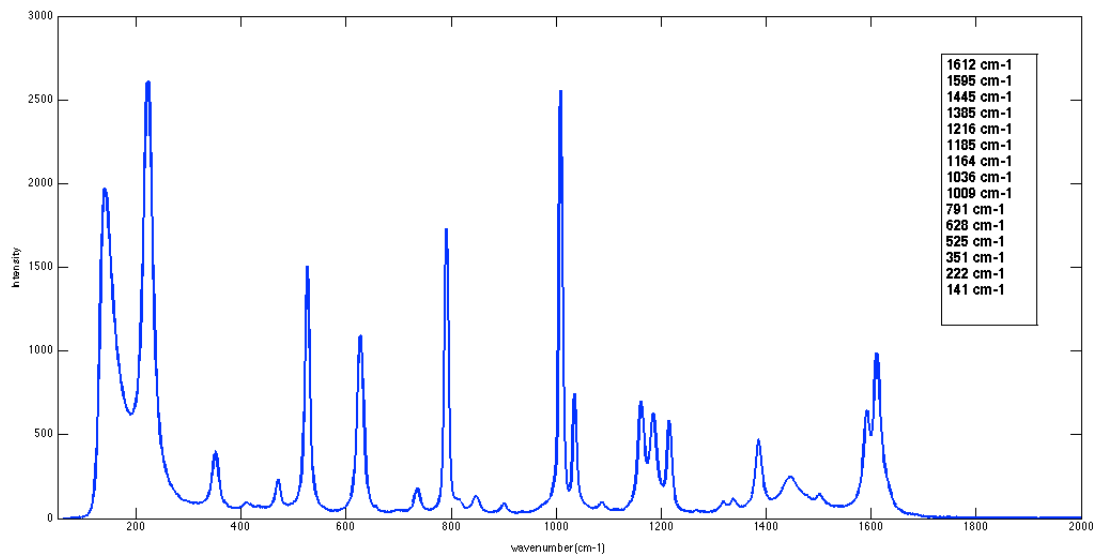
The spectrum of toluene has been measured using the implemented system; the acquired spectrum of this chemical has been validated by comparing it with spectrum published in the Spectral Database for Organic Compounds (SDBS)<sup>27</sup>; this database is managed by National Institute of Advanced Industrial Science and technology in Japan (AIST); figures (6.2.a) and (6.2.b) shows the main Raman shifts in the published and the measured spectrum for toluene.

As shown from these figures, very good spectral matching in the range of  $\pm 5\text{cm}^{-1}$  between the measured and the published spectrums is observed. Based on that it is concluded that the implemented Raman system in this work can produce valid and trusted data. On the other hand, the measured spectrums of BT, dodecane and 1-methylnaphthalene, which will be used later, shows very good spectral matching in the range of  $\pm 5\text{cm}^{-1}$  with the published spectra of these chemicals; this provides a further evidence of the validity of the acquired spectra. It is important to mention here that the

current system successfully measured the Raman spectra for liquids such as toluene, dodecane and 1-methylnaphthalene and the Raman spectra for solids such as BT. However, this system couldn't produce the Raman spectra for gases and metals.



(a)



(b)

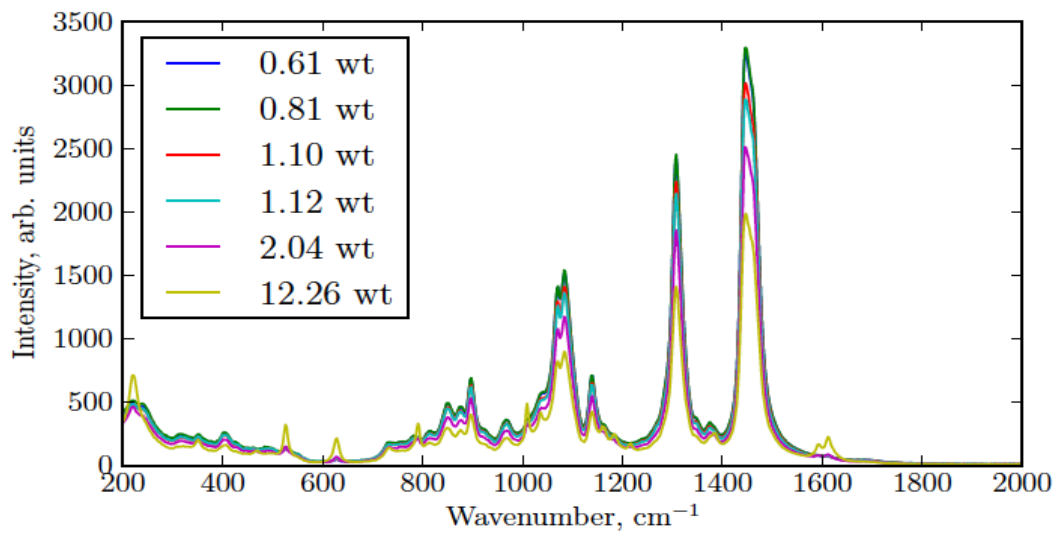
**Figure 6.2: (a) Toluene spectrum published in SDBS; (b) Toluene spectrum acquired by the implemented Raman system.**



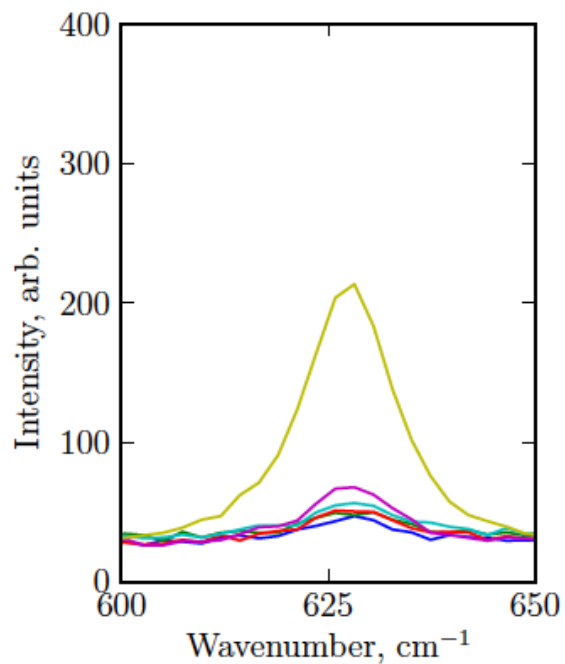
### 6.3 Spectral Calibration Curve For Quantitative Analysis

As mentioned earlier, Raman spectroscopy can be used for quantitative analysis, even for multicomponent mixtures; Quantitative results can be achieved by fitting a calibration curve between the analyte concentration and the measured Raman intensity of a specific band. The best band to be chosen in the analysis should be the strongest unique band for the analyte under investigation. Either the peak height or the peak area can be used as a basis of quantitative analysis.

The Raman technique is easily used to measure high concentrations of solid, liquid or aqueous analytes with little or no sample preparation<sup>28</sup>. Previously, however, the technique was assumed to be not sufficiently sensitive for quantitation of relatively low concentrations samples because of the inherent weak nature of the Raman signal<sup>28</sup>. This limitation could be overcome by improving the S/N ratio by extending the integration time of the analysis and then normalizing the obtained intensity with respect to the integration time<sup>28</sup>. In this work, a calibration curve of toluene / dodecane mixture has been established; a series of toluene in dodecane mixtures have been prepared; the mixtures concentrations are 12.26 wt.%, 2.04 wt.%, 1.12 wt.%, 1.10 wt.%, 0.81 wt.% and 0.61 wt.%. The height of unique toluene Raman band at  $628\text{ cm}^{-1}$  has been used as the basis for the analysis; figure (6.3.a) depicts the Raman spectra of toluene / dodecane mixture at different concentrations; the spectra have been obtained using 3 second of integration time, no averaging of the data and 0 boxcar width; figure (6.3.b) shows a zoomed in portion around the unique  $628\text{ cm}^{-1}$  band. Lower than 0.61 wt.% concentration of toluene, the signal couldn't be distinguished from the noise; therefore, 0.61 wt.% is the minimum detectable limit of toluene in dodecane mixture. The sensitivity of the detection limit could be enhanced by increasing the integration time and normalizing the intensity with respect to the used integration time; this route hasn't be investigated. The height of the  $628\text{ cm}^{-1}$  peak represented by its intensity is plotted vs. the concentration of toluene as depicted in figure (6.4). The value of the regression coefficient ( $r^2$ ) shows that the acquired Raman intensity vs. concentration, in the range (0.6-12 wt.%), can be accurately fitted using linear model. In the future, more points between 2 and 12 wt.% should be measured to confirm this conclusion.



(a)



(b)

**Figure 6.3: (a) Raman spectra of toluene in dodecane mixtures in the range of (0 – 12 wt.%); (b) a zoomed in region of the 628  $\text{cm}^{-1}$  unique toluene band**

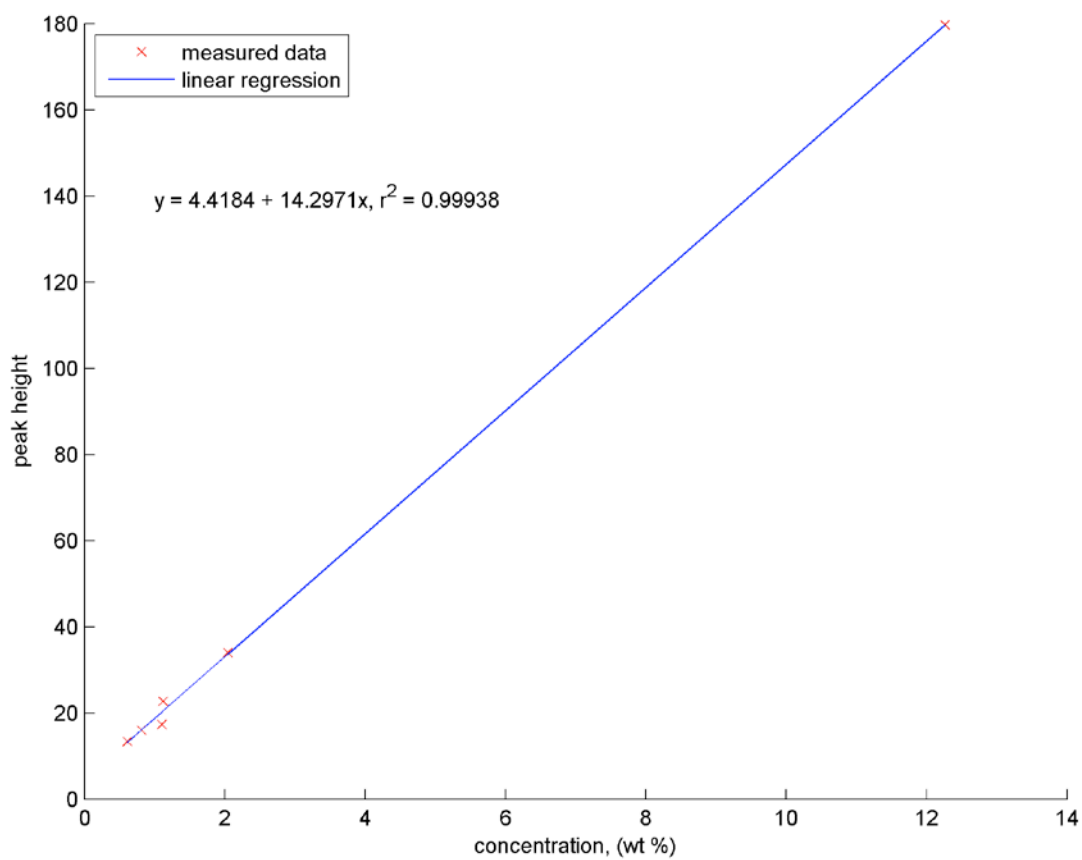


**Figure 6.4: The height of the 628 cm<sup>-1</sup> peak vs. toluene concentration**

## 6.3 HDS Reaction of BT

### 6.3.1 Multivariate Analysis

The online Raman spectra are composed of three-variable dataset; these variables are the wavenumbers, the intensity and the time; figure (6.5) shows the baseline corrected data for one of HDS reactions of BT; it is extremely complicated to reveal the spectral changes associated with this reaction due to the 3-dimensional nature of the data which contains thousands of spectrums.

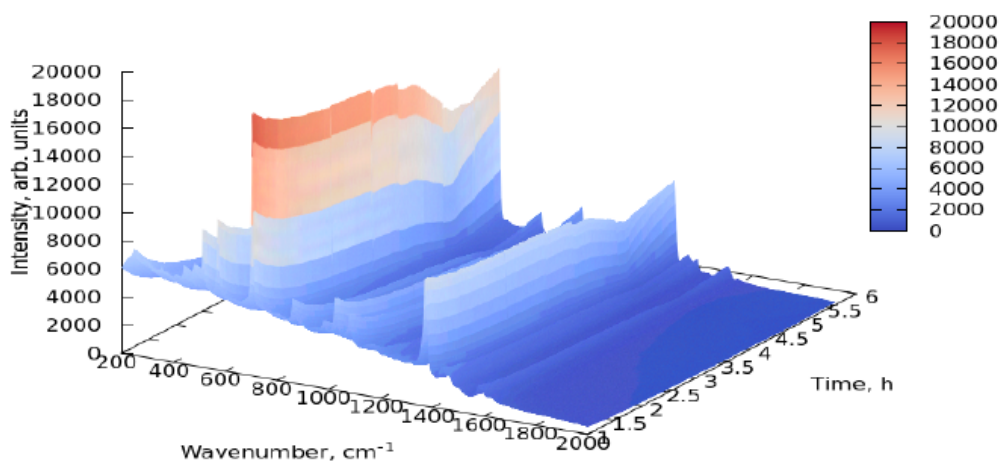
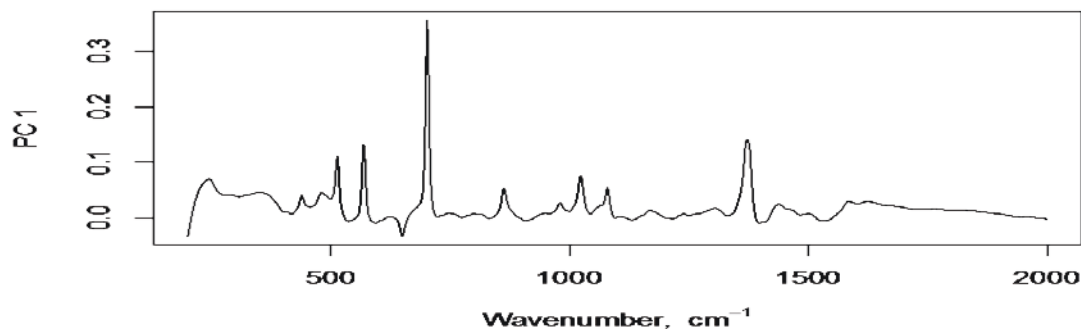


**Figure 6.5: Three-dimensional plot of on-line Raman baseline corrected spectra for one of HDS reaction of BT (figure courtesy of Michal Nipcon).**

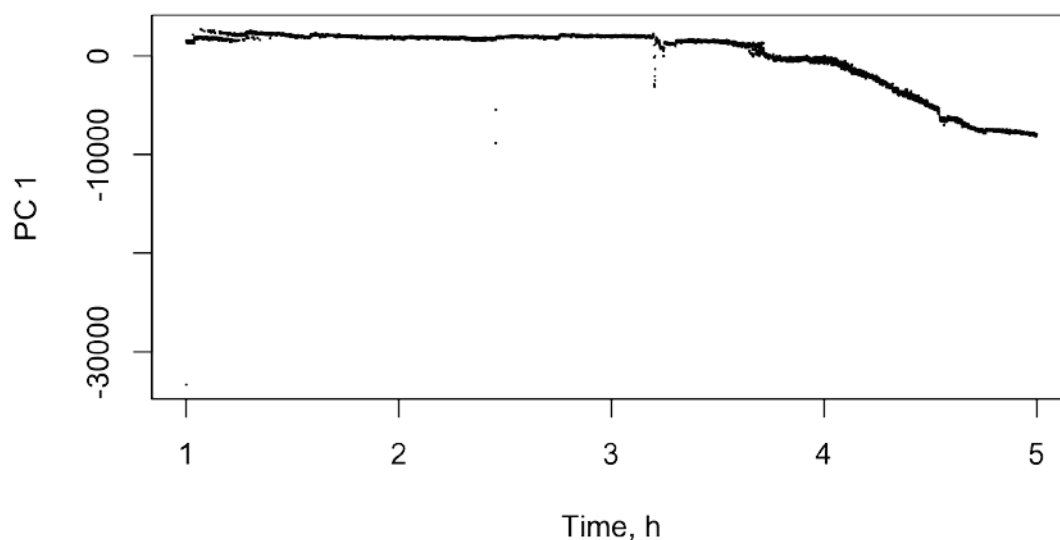
Thus, principal component analysis (PCA) has been used as multivariate method for interpretation of the online spectra of chemical reactions; the PCA method provide a powerful tool to reveal the inherent structure of the data, to reduce the dimensionality of the data by finding alternative coordinates called the principal components (PCs) and to find the pattern, groupings and the outliers<sup>29</sup>. The PCA involves the transformation of thousands of correlated variables such as Raman shift into uncorrelated principal components<sup>29</sup>. In PCA, the uncorrelated data such as Raman spectra is contained in a matrix where the observations, which are the individual spectrum taken at each point in

time, are held in different rows and the variables, which are the wavenumbers, are held in different columns. This matrix is modeled by PCs; each PC is comprised of a scores vector and a loadings vector. For continuous types of data, such as in the case of monitoring a chemical reaction, thousands of spectra are acquired over the course of an experiment. The loadings of PC1 describes the common spectral profile for these spectra over time and the scores of PC1 account for how much each individual spectrum has of that common profile. Each individual spectrum could be thought as separate sample. The largest variance in the data is explained by the first principal component PC1 and the next largest variance is explained by the second principal component PC2 and so on until the whole data variance is explained<sup>29</sup>. Prior to performing PCA on the data, some pre-processing steps may be required; these steps include data centering and scaling. Data centering means to shift the data to be zero centered and it is important to focus on the relative variation between the spectra rather than to see the absolute variation; the scaling means to scale the variables to have a unit variance.

PCA has been applied on the data set that was used to prepare figure (6.5). The reaction data was analyzed over a (200-2000)  $\text{cm}^{-1}$  spectral range. It should be noted that PCA was not done on the heating or cooling phases of the reaction. Figure (6.6.a) presents the loading of PC1 vs. wavenumber while figure (6.6.b) shows the scores of PC1 vs. time.



(a)



(b)

**Figure (6.6): (a) the loading of PC1 vs. wavenumbers; (b) the scores of PC1 vs. time. (200-2000  $\text{cm}^{-1}$  range)**

The loading of PC1 as shown in figure (6.6.a) describes the common spectral profile during the whole reaction time and the score plot (6.6.b) accounts for the value of that loading in each observation at specific time. For example, the peak at  $701\text{cm}^{-1}$  has the highest loading. Inspecting the trend of the scores, it is obvious that the scores declines with time and this is interpreted by intensity drop of the  $701\text{ cm}^{-1}$  peak. In chemical terms, this decrease is consistent with a drop in the concentration of chemical bond assigned to this peak. In order to decide how many PCs are required to explain all variance in the data, the scree plot of the total variance explained by each PC is depicted in figure (6.7).

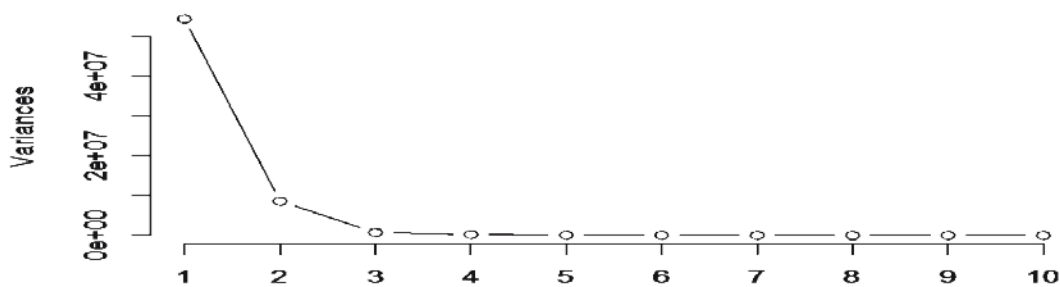


**Figure (6.7): scree plot of total variance described by each PC (200-2000  $\text{cm}^{-1}$  range).**

As shown from figure (6.7), most the variance is explained by PC1 and the then by PC2. On the other hand, PC3 doesn't explain any variance and so on with the other PCs; thus, it is concluded that PC1 and PC2 are sufficient to explain all the variation in the data.

### 6.3.2 In-situ HDS Reaction of BT

The HDS reaction of 1 gram of 2 wt.% of BT in 1-methylnaphthalene using 0.04 gram of pelleted DN-200 catalyst has been conducted in the hot stage reactor; the on-line Raman spectra have been recorded during the reaction. The Raman spectra were collected for the liquid phase of the reaction since this system can only measure the spectra for liquid phase but not the gas phase. The spectra have been acquired via the p-polarized channel using 5 second integration time, 2 scan to average and 0 boxcar width. The reaction was conducted at 290°C and 2.5 MPa of hydrogen pressure for 4 hours. The reaction time was selected based on the ex-situ experiments that showed more than 95% conversion of BT at 4 hours reaction time. This reaction has been repeated three times to check the reproducibility of the results.

The collected Raman spectra have been baseline corrected to remove the fluorescence. The Raman spectra during the reaction phase have been only analyzed while the Raman spectra collected during the heating and cooling phases of the reaction have been omitted from analysis. Moreover, the spectrum of the reaction feed mixture has been subtracted from all the successive spectra in order to see the relative change of the spectra rather

than to see the absolute change; these resulting spectra are called subtracted-baseline corrected spectra.

It is necessary to mention here that with increasing the temperature of the reaction mixture, the baseline shifted up to higher values due to increasing the fluorescence emission and shifted down upon cooling; on the other hand, it is noticed that there are no shifts in the bands positions due to heating or cooling.

The proposed mechanisms for HDS reaction of BT suggest that the BT can be desulfurized to ethylbenzene (EB) via two routes: via direct cleavage of the sulfur-carbon bond (C-S) through hydrogenolysis reaction or via hydrogenation of carbon-carbon unsaturated bond in the thiophene ring; the aforementioned figure (2.1) shows the proposed mechanisms. Therefore, during in-situ reactions we suppose to observe an intensity drop in the Raman shifts associated with both the C-S and C=C bonds, and a growth in the Raman shifts associated with the formation of methyl groups (-CH<sub>3</sub>).

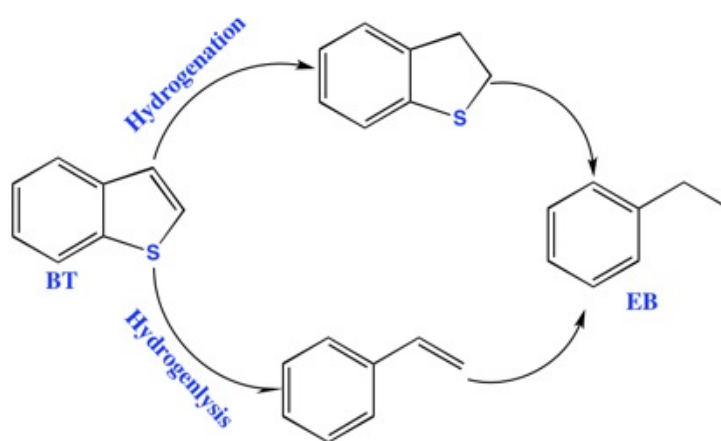


**Figure (2.1): Proposed mechanisms for HDS reaction of BT**

PCA has been performed on the subtracted-baseline corrected spectra in the range 200-2000  $\text{cm}^{-1}$ ; an example of this analysis is depicted in the aforementioned figure (6.6). In order to enhance the sensitivity of the PCA, the original spectral range (200-2000)  $\text{cm}^{-1}$  has been divided into three spectral regions that include the active spectral change; these regions are: (1) 450-830  $\text{cm}^{-1}$ , (2) 830-1100  $\text{cm}^{-1}$ , and (3) 1150-1600  $\text{cm}^{-1}$ ; the PCA has been performed independently over these regions. By performing the PCA over narrower



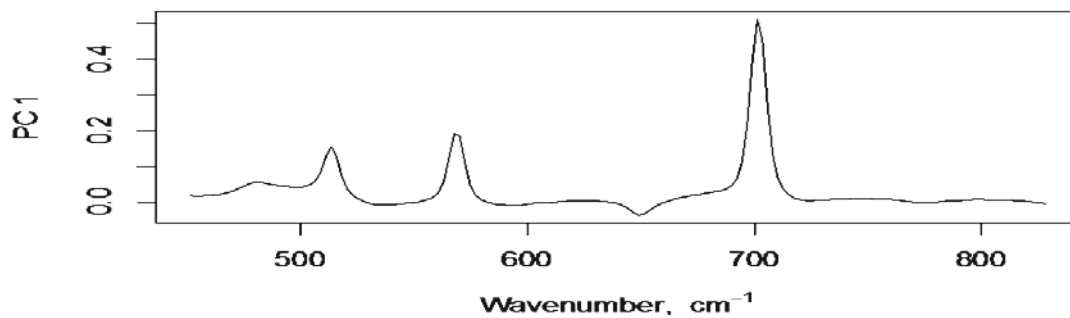
spectral regions, the sensitivity of the analysis is greatly enhanced because the PCA explains the variation in the data using a relatively small number of variables (wavenumbers) which maximizes the spectral resolution of the analysis. This technique is helpful when there is a complex background from a solvent that overlaps with active ingredients of the reaction, such as in the case of BT and 1-Methylnaphthalene, or when detection is difficult due low analyte concentration. PCA has been used to discriminate between very close species of microorganisms which have very similar spectral features<sup>29</sup>. Table (6.1) lists the Raman shifts for benzothiophene (BT), 1-Methylnaphthalene and ethylbenzene (EB); these values have been confirmed by other studies<sup>27,30-32</sup>; the analysis is based on tracking the major Raman shifts that are unique for BT or EB and not present in 1-Methylnaphthalene, or tracking the change in the intensity of major Raman bands that are common.

**Table 6.1: Raman shifts for BT, 1-Methylnaphthalene and EB; w: weak, s: strong, m: medium and v: very.**

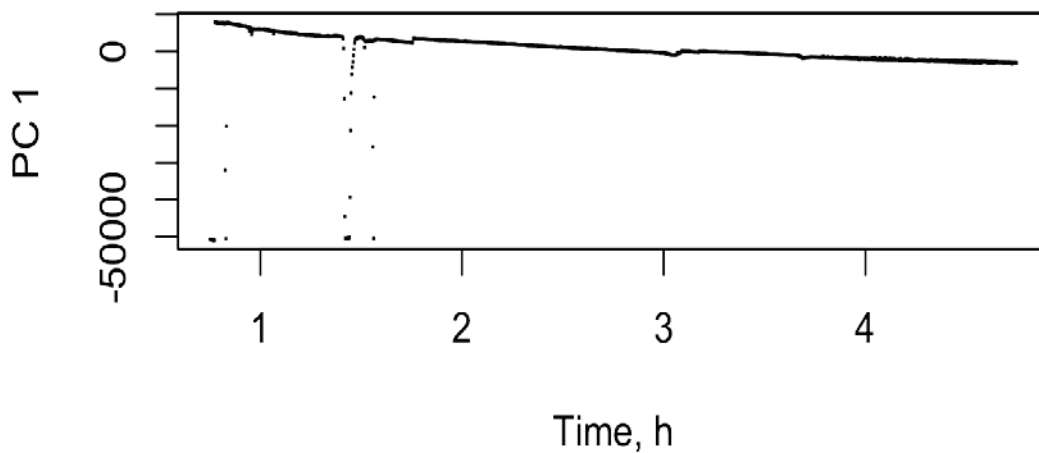
Compound	1-Methynaphthalene	BT	EB
Raman shifts cm <sup>-1</sup>	1629 v.w	1590 v.w	1607 s
	1585 m	1556 s	1445 w
	1517 v.w	1495 s	1373 v.w <sup>30</sup>
	1471 w	1455 w	1330 w
	1436 w	1422 v.w	1205 s
	1382 v.s	1345 w	1155 w
	1273 v.w	1315	1060 v.w
	1250 v.w	1263 v.w	1032 s
	1170 w	1207 w	1005 v.s
	1148 w	1132 v.w	960 w
	1083 m	1090 v.w	771 s
	1025 m	1055 m	698 w <sup>32</sup>
	986 w	1015 v.s	620 m
	865 m	865 s	555 v.w
	799 v.w	795 v.s	480 w
	741 v.w	706 v.s	
	708 v.s	525 v.w	
	572 s	492 s	
	516 s	475 w	
	482 m	417 w	
444 w			
415 w			

### 6.3.2.1 Raman Activity In 450-830 $\text{cm}^{-1}$ Region

The loading vs. the wavenumbers for PC1 is plotted in figure (6.8.a) and the scores vs. time is plotted in figure (6.8.b); the scree plot is depicted in figure (6.9).



(a)



(b)

**Figure 6.8: (a) the loading of PC1 vs. wavenumbers; (b) the scores of PC1 vs. time. (450-830  $\text{cm}^{-1}$  range)**

PC1 describes the general trend in the data; it is obvious from the above figures that there is intensity drop in Raman shifts located at 701, 568, 514 and 480  $\text{cm}^{-1}$ ; on the other hand, there is intensity increase in the 647 $\text{cm}^{-1}$  weak band. The drop in the strong 701 $\text{cm}^{-1}$  band, which is attributed to C-S stretching<sup>33</sup>, confirms the sulfur removal through out the reaction; an evidence for hydrogenation of unsaturated carbon-carbon bond is the increase in peak located at 647  $\text{cm}^{-1}$  since this peak is assigned to  $\text{CH}_2$  twisting mode<sup>34</sup>. Moreover, the decline in the 568 and 514  $\text{cm}^{-1}$  Raman shifts proposes a consumption of 1-methylnaphthalene because these peaks are unique for 1- methylnaphthalene.

From figure (6.9), it is concluded that two PCs are enough to explain all variation in the data since PC3 explain zero variance.

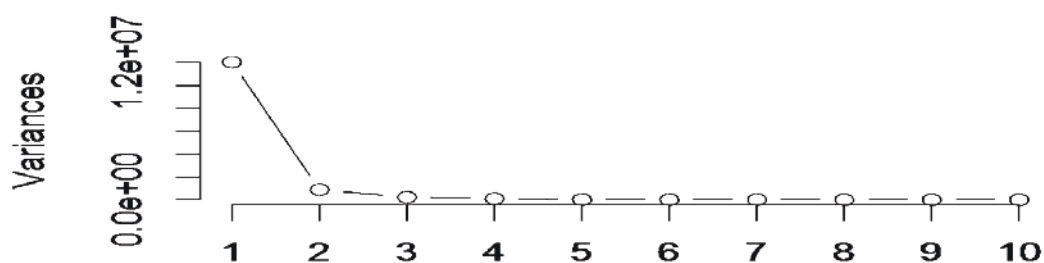
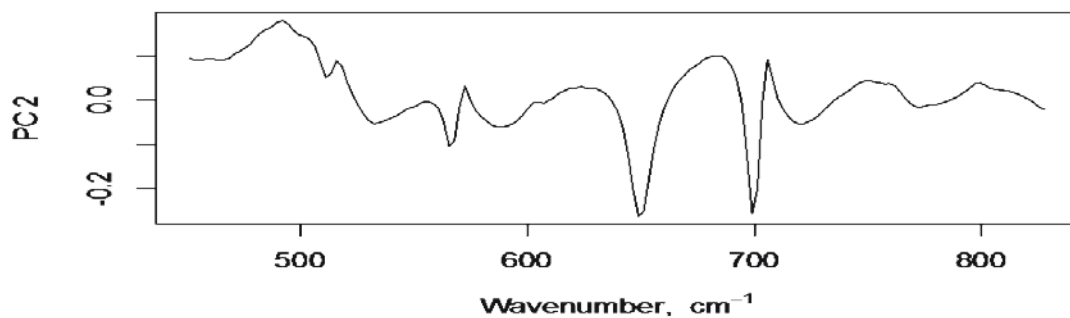


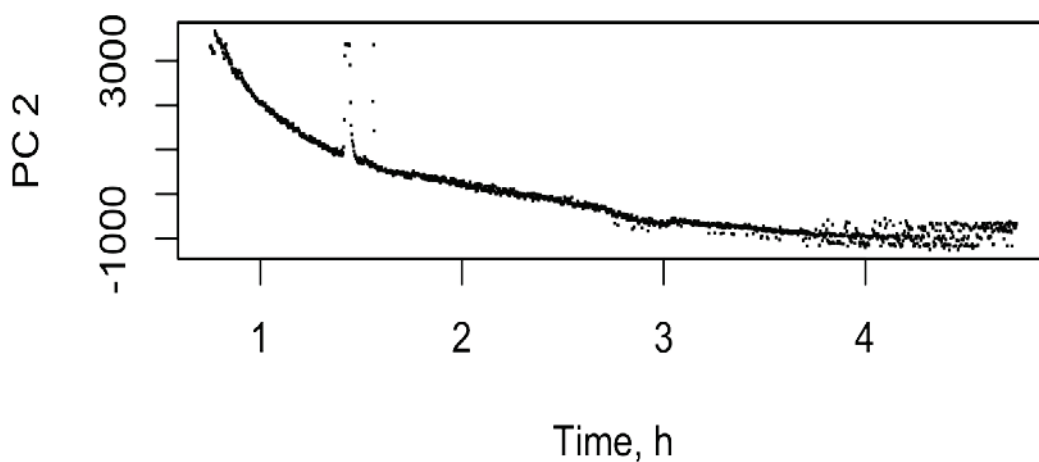
**Figure 6.9: Scree plot of total variance described by each PC (450-830  $\text{cm}^{-1}$  range)**

The unexplained part of the data could be interpreted using PC2. Therefore, the loading and the scores of PC2 are plotted in figure (6.10).

More detailed information could be extracted from PC2; for example, the strongest peak at 701  $\text{cm}^{-1}$ , which was previously mentioned in figure (6.8), is resolved into two close bands at 703 and 698  $\text{cm}^{-1}$ ; this peak separation is not observed when the PCA has been performed on the original spectral range (200-2000)  $\text{cm}^{-1}$  that provides a good example of how narrowing the processed spectral range can enhance the PCA sensitivity and extract more chemical information.



(a)



(b)

**Figure 6.10: (a) the loading of PC1 vs. wavenumbers; (b) the scores of PC1 vs. time. (450-830  $\text{cm}^{-1}$  range)**

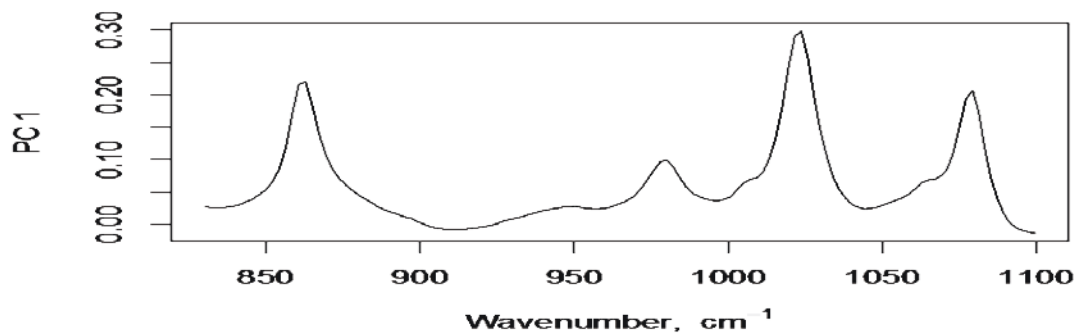
From the score plot (6.10.b), the 698  $\text{cm}^{-1}$  band, which is assigned to the formation of ethylbenzene<sup>32</sup>, strengthens with time while the band at 703  $\text{cm}^{-1}$ , which was previously assigned to C-S stretching, declines with time. Resolving of close peaks is observed again around 568  $\text{cm}^{-1}$  band; this peak is separated into two bands located at 565 and 570  $\text{cm}^{-1}$ . The 565  $\text{cm}^{-1}$  peak, which could be assigned to ethylbenzene formation<sup>32</sup>, develops with time while the 570  $\text{cm}^{-1}$  peak, which was previously attributed to the consumption of 1- methyl-naphthalene, decreases with time. Also, the peak at 647  $\text{cm}^{-1}$  gets stronger

while an intensity drop is observed for 514  $\text{cm}^{-1}$  band; these results are consistent with the PC1 analysis. Furthermore, of particular importance is the decline in 492  $\text{cm}^{-1}$  band; this peak is assigned to in-plane deformation of thiophene ring denoted as  $\alpha$  (C-S-C)<sup>31</sup>. This result provides more evidence of sulfur removal. The drop in the 795  $\text{cm}^{-1}$  shift, which is unique for BT, confirms the consumption of BT. On the other hand, the broad peak at 771 which is unique for EB is attributed to CH<sub>2</sub> rocking<sup>32</sup>, the increase in intensity of this peak confirms the hydrogenation of the unsaturated carbon-carbon bond and the formation of methylene groups (-CH<sub>2</sub>).

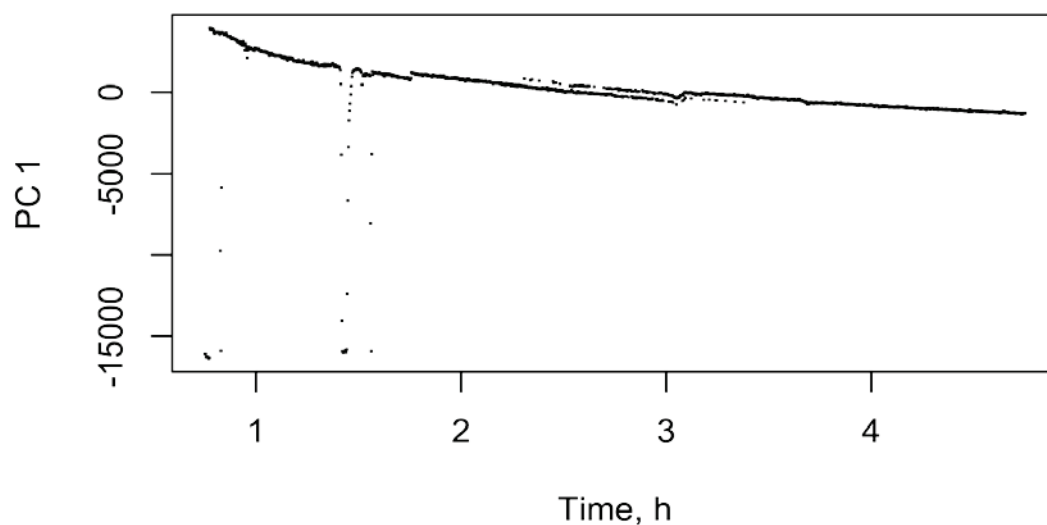
### **6.3.2.2 Raman Activity In 830-1100 $\text{Cm}^{-1}$ Region**

Figures (6.11) and (6.12) show the loading vs. wavenumber and the scores vs. time for PC1 and PC2 respectively.

From PC1 there is a decline in the intense symmetric stretching mode of the aromatic ring located at 1023  $\text{cm}^{-1}$ <sup>35</sup>; this provides an evidence to the unfavorable consumption of the aromatic ring due to hydrogenation reaction. Also, there is a drop in the 863  $\text{cm}^{-1}$  band, which is common between BT and MN, and a drop in 980  $\text{cm}^{-1}$  band and 1079  $\text{cm}^{-1}$  band that are unique for 1-methylnaphthalene; this trend supports the previous conclusion of 1-methylnaphthalene consumption.



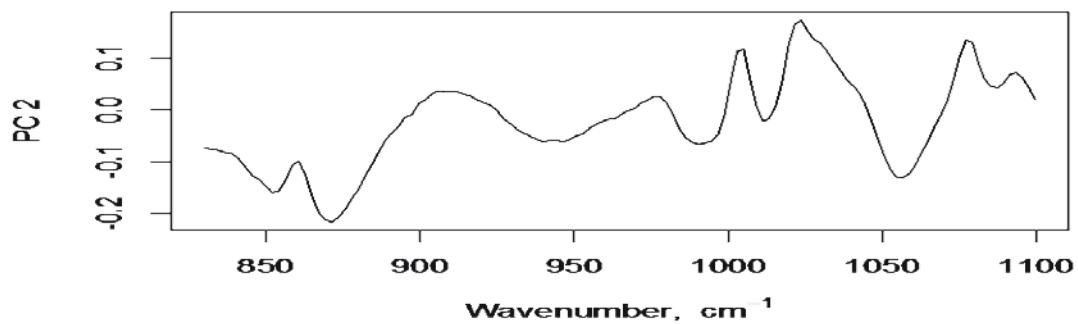
(a)



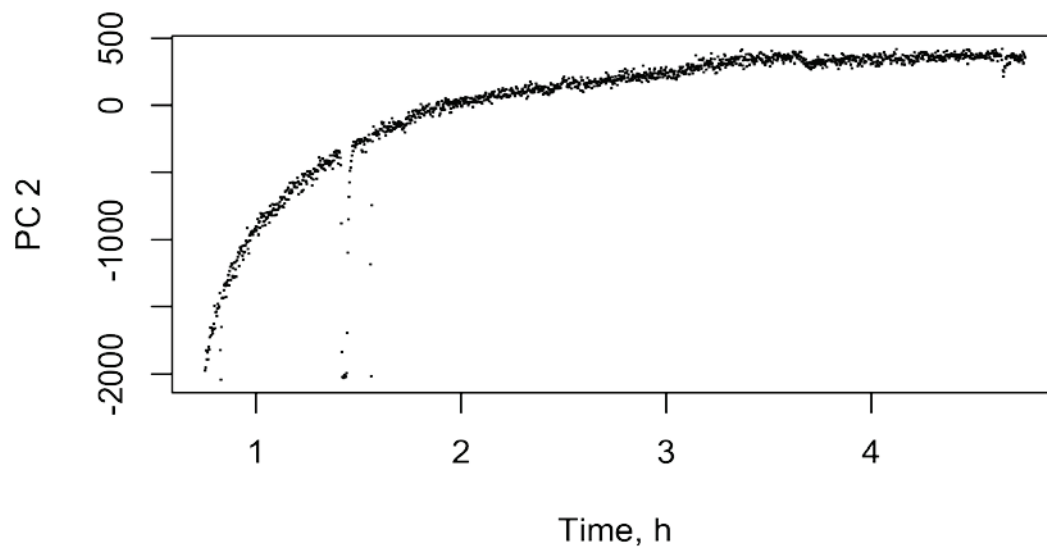
(b)

**Figure (6.11): (a) the loading of PC1 vs. wavenumbers; (b) the scores of PC1 vs. time. (830-1110  $\text{cm}^{-1}$  range)**

On the other hand, the loading of PC2 is confusing since it is not easy to differentiate between the baseline and the peaks which makes the peak assignment a matter of choice, and so, no further comments is made. However, most of the data variability is explained by PC1 as shown by the scree figure (6.13)



(a)



(b)

**Figure (6.12): (a) the loading of PC1 vs. wavenumbers; (b) the scores of PC1 vs. time. (830-1100 cm<sup>-1</sup> range)**

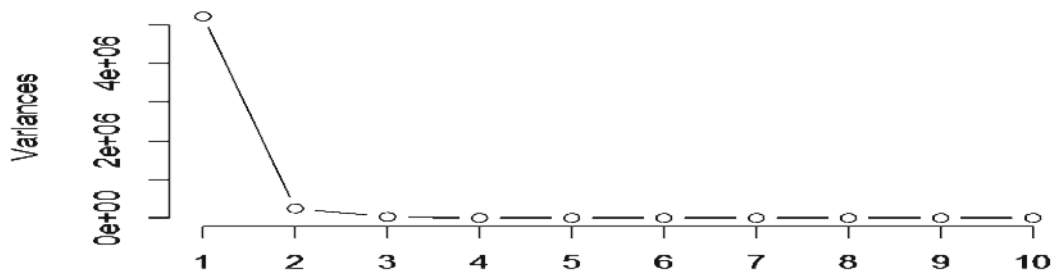


**Figure 6.13: scree plot of total variance described by each PC (830-1100  $\text{cm}^{-1}$  range)**

### 6.3.2.3 Raman Activity In 1150-1650 $\text{Cm}^{-1}$ Region

Two PCs are required to satisfactory explain all the variance in the data in this spectral range as shown in figure (6.14).

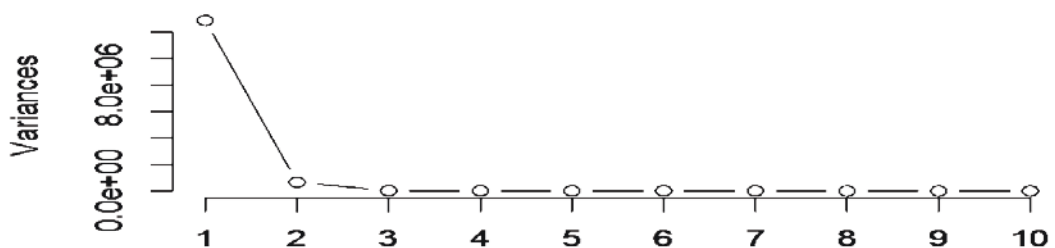
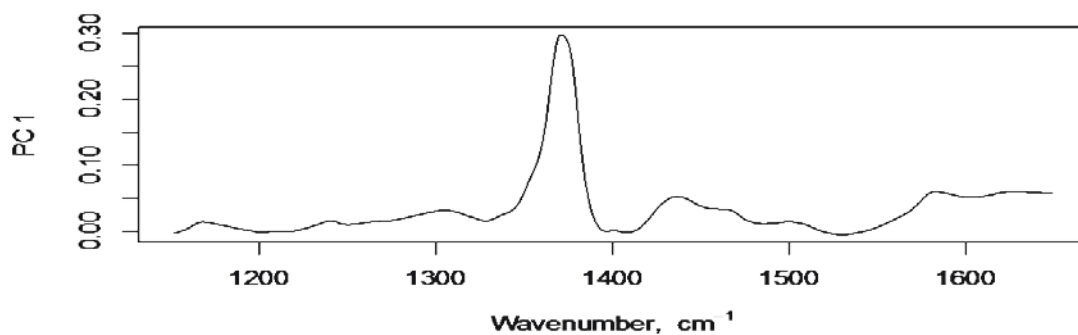


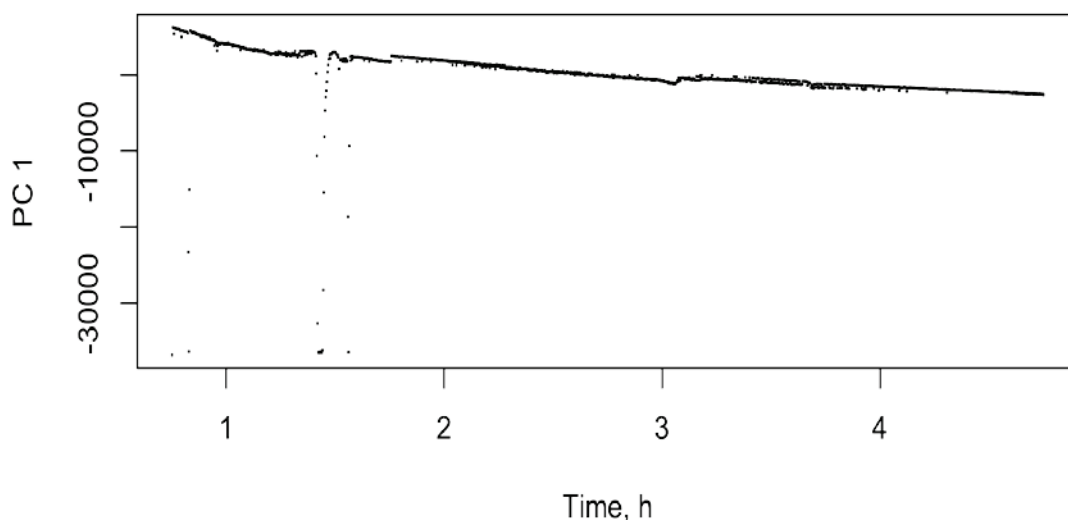
**Figure 6.14: Scree plot of total variance described by each PC (1330-1660  $\text{cm}^{-1}$  range)**

PC1 is used to evaluate a general profile of the data; the loading and the score plots of PC1 are depicted in figure (6.15).





(a)



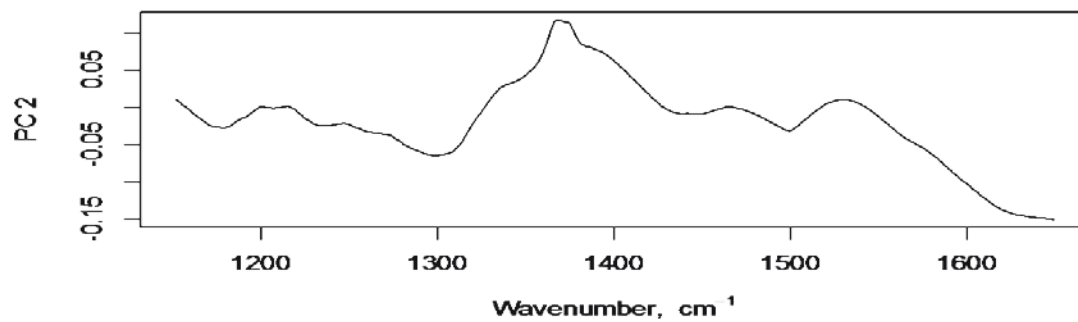
(b)

**Figure 6.15: (a) The loading of PC1 vs. wavenumbers; (b) the scores of PC1 vs. time. (1150-1650  $\text{cm}^{-1}$  range)**

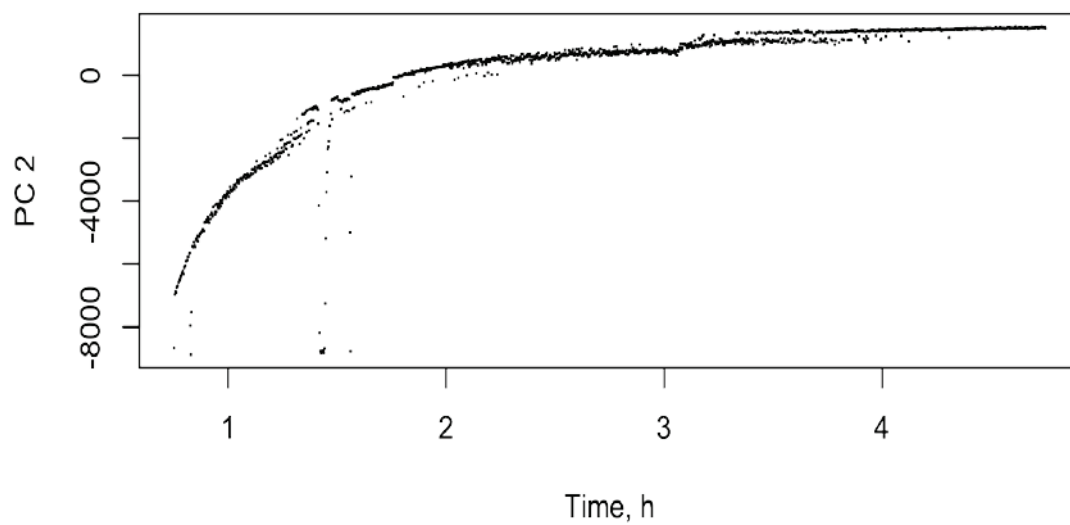
Figure (6.15) show a decay in the strong peak located at  $1372 \text{ cm}^{-1}$ ; there are two possible assignments for this band: the first assignment is the carbon-carbon stretching in aromatic ring<sup>31</sup>; this mode is located at  $1383 \text{ cm}^{-1}$  in 1-methylnaphthalene; the other possible assignment is symmetric deformation in methyl group ( $-\text{CH}_3$ ); the symmetric deformation or umbrella mode fall in the  $1375 \pm 10 \text{ cm}^{-1}$ . Due to the tendency of the  $1372$

$\text{cm}^{-1}$  band to sharpness rather than broadness, it is assigned to the carbon-carbon stretching in aromatic ring since bands of aromatic origin produce sharper peaks while bands of aliphatic origin produce broader peaks<sup>36</sup>. The other very weak bands; which are located at  $1436 \text{ cm}^{-1}$  (carbon-carbon stretching in aromatic ring)<sup>37</sup>,  $1500 \text{ cm}^{-1}$  (carbon-carbon stretching in aromatic ring) and  $1581 \text{ cm}^{-1}$  (carbon-carbon stretching in aromatic ring)<sup>36</sup>; drop in their intensity with time that support, along with the decay in  $1372 \text{ cm}^{-1}$  band, the conclusion of hydrogenation of aromatic rings during the reaction; the undesirable hydrogenation of aromatic rings produces cyclic structure such as isomers of tetrahydro-methylnaphthalene

From PC2 in figure (6.16), the improvement in the broad peak at  $1205 \text{ cm}^{-1}$  confirms the formation of EB; this band is common between BT and EB but it is strong in EB and weak in BT. The broad peak between  $(1368-1380) \text{ cm}^{-1}$ , which increases with time, is assigned to  $-\text{CH}_3$  symmetric deformation (umbrella) mode; the higher limit of the peak ( $1380 \text{ cm}^{-1}$ ) proposes a formation of  $-\text{CH}_3$  group attached to  $\text{sp}^2$  carbon (such as methylbenzene) while the lower limit ( $1368 \text{ cm}^{-1}$ ) proposes a formation of gem-dimethyl group (such as isopropylbenzene)<sup>36</sup>. Finally, the drop in the  $1500 \text{ cm}^{-1}$  Raman shift with time supports the previous conclusion of aromatic ring hydrogenation.



(a)



(b)

**Figure 6.16: (a) The loading of PC2 vs. wavenumbers; (b) the scores of PC2 vs. time. (1150-1650  $\text{cm}^{-1}$  range)**

### **6.3.3 Products Analysis**

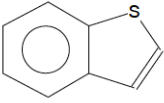
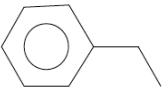
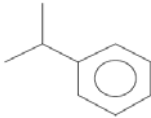
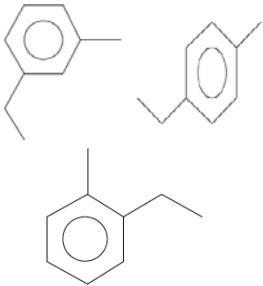
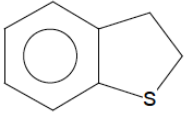
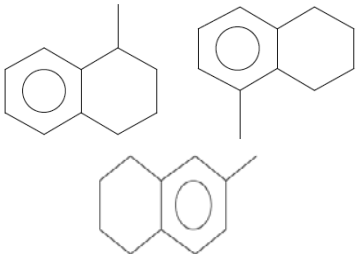
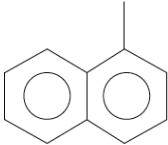
#### **6.3.3.1 Product Analysis Of The Ex-Situ Reactions**

Prior to the in-situ reactions that have been discussed in the previous section (6.3.2), a set of ex-situ HDS reaction of BT had been conducted in the batch reactor; the ex-situ reactions had been conducted for 20, 40, 60, 80, 120, 240 and 360 min at the same conditions of the in-situ runs (i.e. 290 °C, 2.5 MPa of Hydrogen pressure and reaction feed composed of 2 wt.% BT in 1-methylnaphthalene); the reaction products have been analyzed using GC/MS technique.

The GC/MS analysis shows more than 95% conversion of BT at 240 min (4 hour) run; this is the reason why 4 hours has been chosen as a reaction time for in-situ experiments; table (6.2) list reaction products for the ex-situ run after 4 hours of reaction.

From table (6.2), it could be concluded that the BT has been reacted to EB and at the same time other undesirable reactions such as hydrogenation of the solvent (1-methylnaphthalen) have been occurred. Furthermore, no styrene has been detected in any of the ex-situ runs that may support the claim that styrene is an intermediate that readily consumed upon formation. Moreover, a trace amount of 2,3-dihydro- benzothiophene has been found which confirms the hydrogenation pathway during the HDS reaction of BT.

**Table 6.2: Products analyses for the ex-situ run after 4 hours of reaction**

Compound	Molecular structure
Benzothiophene	
Ethylbenzene	
Isopropylbenzene	
1-ethyl-3-methyl-benzene, 1-ethyl-4-methyl-benzene & 1-ethyl-2-methyl-benzene,	
2,3-dihydro- benzothiophene	
1,2,3,4-tetrahydro-1-methyl-naphthalene 1,2,3,4-tetrahydro-5-methyl-naphthalene & 1,2,3,4-tetrahydro-6-methyl-naphthalene	
1-methylnaphthalen	

### 6.3.3.2 Product Analysis Of The In-Situ Reactions

In order to validate the results obtained in the in-situ runs, the reaction products of the in-situ experiments, which have been discussed in section (6.3.2), have been analyzed; the analysis shows the same chemical compounds as in table (6.2). More than 98% conversion of BT has been achieved in the three in-situ reactions; the consumption of BT has been pointed out in the PCA by the drop in the stretching and bending modes of carbon-sulfur bonds and by the drop of the unique bands of BT. About 85% fractional yield of EB has been formed; this has been extracted by the increase in the intensity of vibrational bands associated with  $-CH_3$  and  $-CH_2$  groups and by the increase in the unique bands of EB. On the other hand, no styrene has been formed and a trace amount of 2,3-dihydro-benzothiophene has been produced that agree with the results obtained ex-situ. Finally, about 14% of 1-methylnaphthalene have been converted to isomers of 1,2,3,4-tetrahydro-methyl-naphthalene (cyclic structure); this provide an important evidence for the hydrogenation capability of this catalyst over desulfurization capability as mentioned in the literature review; the hydrogenation of the aromatic ring and the formation of cyclic structure have been deduced from the PCA as mentioned earlier.

## Conclusion

In this work, an in-situ analytical tool for probing the chemical reactions has been built and validated. The system has been developed to track the Raman bands during the carbonization of petroleum pitch. The system elements, namely the laser source and the spectrometer have been selected carefully to be compatible with high fluorescent nature of the petroleum pitch. The HDS reaction of BT has been used as a model reaction to validate the system. The interpretation of the collected spectra during the reaction by the means of PCA has shown a decline in the Raman bands attributed to the hydrodesulfurization of BT and to the dearomatization of the solvent; on the other hand, the PCA has shown an improvement in the Raman bands associated with formation of ethylbenzene. These results are compatible with those results obtained at *ex-situ* conditions. It has been demonstrated that the Raman spectroscopy along with the principal component analysis is a powerful technique to monitor chemical reactions and to elucidate the reaction mechanism. Furthermore, due to the categorization potential of PCA, the Raman spectroscopy along with PCA could be used for quality and process control applications.

## Bibliography

1. Bagheri, S. R. *Mesophase Formation in Heavy Oil*. PhD dissertation, University of Alberta, Chemical & Material Engineering Department, Fall (2012).
2. Mochida, I. Molecular Assembly Of Mesophase And Isotropic Pitches At Their Fused States. *Carbon* **30**, 1019–1024 (1992).
3. Marsh, H. & Latham, C. S. The Chemistry of Mesophase Formation. *ACS Symposium Series* **29**, 1-28 (1986).
4. Angell, C. L. & Lewis, I. C. Raman Spectroscopy of Mesophase Pitches. *Carbon* **16**, 431–432 (1978).
5. Ferraro, J. R., Nakamoto, K. & Brown, C. W. *Introductory Raman Spectroscopy Ch.1* (Elsevier, second edition, 2003).
6. Adar, F. *Evolution and Revolution of Raman Instrumentation-Application of Available Technologies to Spectroscopy and Microscopy* (Jobin Yvon Inc., Edison, New Jersey, 2001).
7. Pelletier, M. J. & Pelletier, C. C. *Reference Module in Chemistry, Molecular Sciences and Chemical Engineering, Raman Spectroscopy: Instrumentation*. (Elsevier, 2005).
8. Ferraro, J. R., Nakamoto, K. & Brown, C. W. *Introductory Raman Spectroscopy Ch.2* (Elsevier, second edition, 2003).
9. Mochida, I., Korai, Y., Ku, C.-H., Watanabe, F. & Sakai, Y. Chemistry of synthesis, structure, preparation and application of aromatic-derived mesophase pitch. *Carbon* **38**, 305–328 (2000).
10. Wiehe, I. A. A Phase-Separation Kinetic Model For Coke Separation. *Ind. Eng. Chem. Res* **32**, 2447–2454 (1993).
11. Marsh, H., Martínez-Escandell, M. & Rodríguez-Reinoso, F. Semicokes From Pitch Pyrolysis: Mechanisms And Kinetics. *Carbon*. **37**, 363–390 (1999).
12. Zhou, H. *et al.* Catalytic graphitization of PAN-based carbon fibers with electrodeposited Ni-Fe alloy. *Trans. Nonferrous Met. Soc. China* **21**, 581–587 (2011).
13. Scholte, P. *Arsenic Effects On A NiMo/Al<sub>2</sub>O<sub>3</sub> Hydrotreating Catalyst*, Master Thesis, University of Alberta, Chemical & Material Engineering Department, Spring (2012).



14. Shi, L., Tin, K. C., Wong, N. B., Wu, X. Z. & Li, C. L. Kinetics And Mechanism Of Benzothiophene Hydrodesulfurization Over NiO-MoO/Y-Al<sub>2</sub>O<sub>3</sub> Commercial Catalyst. *Fuel Science and Technology International* **14**, 767-784 (1996).
15. Wang, H. & Prins, R. HDS Of Benzothiophene And Dihydrobenzothiophene Over Sulfided Mo/γ-Al<sub>2</sub>O<sub>3</sub>. *Appl. Catal. A Gen.* **350**, 191–196 (2008).
16. Ishihara, A. et al. Effect Of Solvent On HDS Of BT. *Journal of Catalysis* **140**, 184-189 (1993).
17. Mayo, D.W., Miller, F.A. & Hannah, R.W. *Course Notes On The Interpretation Of Infrared And Raman Spectra Ch1* (John Wiley & Sons, Inc., Hoboken, New Jersey, 2003).
18. Larkin, P. *Infrared And Raman Spectroscopy: Principles And Spectral Interpretation Ch2* (Elsevier, first edition, 2011).
19. Vankeirsbilck, T., Vercauteren, A., Baeyens, W. & Weken, G. Van Der. Applications Of Raman Spectroscopy In Pharmaceutical Analysis. *Trends in Analytical Chemistry* **21**, 869–877 (2002).
20. Larkin, P. *Infrared And Raman Spectroscopy: Principles And Spectral Interpretation Ch3* (Elsevier, first edition, 2011).
21. Office of Environmental Health & Safety. Laser Safety Manual. University of Alberta, April (2003).
22. Rahimi, P. et al. Investigation Of Coking Propensity Of Narrow Cut Fractions From Athabasca Bitumen Using Hot-Stage Microscopy. *Energy & Fuels* **12**, 1020–1030 (1998).
23. Pemberton, J. E. & Sobocinski, R. L. Raman Spectroscopy with Helium-Neon Laser Excitation and Charge-Coupled Device Detection. *J. AM. Chem. Soc.* **111**, 432–434 (1989).
24. Zhang, Z.-M., Chen, S. & Liang, Y.-Z. Baseline Correction Using Adaptive Iteratively Reweighted Penalized Least Squares. *Analyst* **135**, 1138–1146 (2010).
25. Zhang, Z.-M. et al. An Intelligent Background-Correction Algorithm For Highly Fluorescent Samples In Raman Spectroscopy. *J. Raman Spectrosc.* **41**, 659–669 (2009).
26. Cobas, J. C., Bernstein, M. a, Martín-Pastor, M. & Tahoces, P. G. A New General-Purpose Fully Automatic Baseline-Correction Procedure For 1D And 2D NMR Data. *J. Magn. Reson.* **183**, 145–151 (2006).

27. Tanabe, K. & Hiraishi, J. Spectral Data Base For Organic Compounds SDBS. [Http://sdb.sdb.aist.go.jp/sdb/cgi-bin/cre\\_index.cgi](http://sdb.sdb.aist.go.jp/sdb/cgi-bin/cre_index.cgi) (2014).
28. Giles, J. H., Gilmore, D. A. & Denton, M. B. Quantitative Analysis Using Raman Spectroscopy Without Spectral Standardization. *J. Raman Spectrosc.* **30**, 767–771 (1999).
29. Mobili, P., Londero, A. & Antoni, G. De. Multivariate Analysis Of Raman Spectra Applied To Microbiology: Discrimination Of Microorganisms At The Species Level. *Revista Mexicana De Fisica* **56**, 378–385 (2010).
30. Fishman, A. I., Klimovitskii, A. E., Skvortsov, A. I. & Remizov, A. B. The Vibrational Spectra And Conformations Of Ethylbenzene. *Spectrochimica Acta Part A* **60**, 843–853 (2004).
31. Frank, O., Jehliř, J. & Edwards, H. G. M. Raman Spectroscopy As Tool For The Characterization Of Thio-Polyaromatic Hydrocarbons In Organic Minerals. *Spectrochimica Acta Part A* **68**, 1065–1069 (2007).
32. Saunders, J. E. & Lucier, J. J. Infrared And Raman Vibrational Study Of Ethylbenzene , N-Propylbenzene , And Terminal Halogen-Substituted Analogs , 800-50 cm<sup>-1</sup>. *Spectrochimica Acta* **24A**, 2023-2043 (1968).
33. Hampton, C. & Demoin, D. Vibrational Spectroscopy Tutorial: Sulfur And Phosphorus. University Of Missouri, Fall (2010).
34. Bloxham, S., Eicher-lorka, O., Jakubenas, R. & Niaura, G. Surface-enhanced Raman spectroscopy of ethanethiol adsorbed at copper electrode. *Chemija* **13**, 185-189 (2002).
35. Spectrochimica, E. & Part, A. Remote fiber optic Raman analysis of benzene , toluene , and ethylbenzene in mock petroleum fuels using partial least squares regression analysis. **52**, (1996).
36. Mayo, D.W., Miller, F.A. & Hannah, R.W. *Course Notes On The Interpretation Of Infrared And Raman Spectra Ch2* (John Wiley & Sons, Inc., Hoboken, New Jersey, 2003).
37. Novak, P. *et al.* In-Line Reaction Monitoring Of Entacapone Synthesis By Raman Spectroscopy And Multivariate Analysis. *J. Pharm. Biomed. Anal.* **54**, 660–666 (2011).